Pro gradu - avhandling

Fysik

First level triggering of diffractively produced low-mass Higgs at The Large Hadron Collider

Fredrik Oljemark

2006

Handledare: FD Kenneth Österberg

Granskare: Prof. Paul Hoyer, Prof. Risto Orava

HELSINGFORS UNIVERSITET
INSTITUTIONEN FÖR FYSIKALISKA VETENSKAPER

PB 64
00014 Helsingfors universitet

Contents

1 Introduction **1**

1.1 Abstract 1

1.2 Motivation 1

1.3 Overview of this thesis 3

1.4 Particle physics primer 3

1.4.1 The Standard Model 3

1.4.2 Diffractive processes 6

1.4.3 Tests of the Standard Model 8

1.4.4 Feynman diagrams 9

1.5 LEP and the LHC 12

1.6 LHC experiments and triggers 13

2 The Higgs boson **16**

2.1 Higgs production 18

2.2 Higgs decay 18

2.3 Pre-LHC Higgs searches 20

2.4 Higgs search at the LHC 21

2.5 Diffractive Higgs-production 22

3 Tools **24**

3.1 CMS/TOTEM L1 trigger 24

3.2 Simulation 25

3.3 Generators for diffractive Higgs 26

4 Results **28**

4.1 Jet E_T calibration 28

4.2 Invariant masses of jet combinations 31

4.3 Muon triggers present and future 34
4.4 A somewhat more massive Higgs 37
4.5 Scalar sum of L1 jet E_T 42
4.6 Back-to-back criterion for the two largest L1 jets 42

5 Conclusions **47**

A Transverse energy correction for L1 jets in CMS **49**
A.1 Abstract 49
A.2 Introduction 49
A.3 Event sample used 50
A.4 Calibration method 51
A.5 Results 53
A.6 Conclusions 56
A.7 Appendix: Calibration functions for different η-intervals 57

Chapter 1

Introduction

1.1 Abstract

The Higgs boson is the only Standard Model particle that has not yet been found. One of the experimentally more favourable production processes at the Large Hadron Collider at CERN for a Higgs boson, in the theoretically favoured low mass range, is the central diffractive process. In this thesis, different first level trigger selection criteria, which use muon and/or jet signatures to retain a significant fraction of diffractive Higgs events while still keeping the accepted event rate at an acceptable level, have been studied. The conclusion of the thesis is that this is feasible using the already existing one and two muon triggers for the Higgs decays to W^+W^- and $b\overline{b}$. In addition, a new trigger combination, one muon plus one jet could enhance the trigger efficiency of the $b\overline{b}$ channel by about 50 % without adding a significant amount of additional background event rate. In addition, a method to correct the first-level measurements of transverse jet energy so as to better correspond to the real transverse jet energy has been developed in the thesis.

1.2 Motivation

To be able to discover the Higgs particle, we must first make sure that a we do not reject them at the lowest trigger level, which has the crudest information on each event it scrutinizes and the highest rate of events to consider. Thus the level-one (L1) triggers that are implemented should be a compromise between having low computational complexity necessary to get a fast save-or-discard decision, reducing the rate enough

so as not to overwhelm the high level trigger, and discriminating between the background and the L1 signatures of all the physics processes we can reasonably expect to learn something about at the Large Hadron Collider (LHC). Being a multidimensional optimization problem, there will not be any globally optimal L1 threshold values that are best for the measurement of all physics processes. Thus every interesting process has to be studied to find the signal efficiency of all the L1 triggers that can discriminate that process from other background processes. By looking at all of these studies, one may obtain the ranges for L1 trigger thresholds within which most of the important physics processes are triggered on with enough efficiency.

Of course, factors like minimum permissible rate reduction are not constant, but depend on the luminosity of the LHC, which will start low and be improved gradually, as the accelerator experts get to know the machine. Therefore the best Higgs-creating subprocesses to trigger on change, as the instantaneous and integrated luminosities grow. The exclusive diffraction Higgs production cross section is predicted to be only around $O(10^{-4})$ of the total Higgs cross section (Ref. [1]). However, exclusive central diffraction has a much lower background and better mass resolution, and will be of interest after the LHC has collected $\mathscr{L} > O(30\ \text{fb}^{-1})$. This does not mean diffractive scalar particle production is of no interest before a few years have gone by, since some extensions of the Standard Model, like supersymmetry, can enhance the Higgs production cross section by a few orders of magnitude (Ref. [2]), or some other unknown scalar particle might be found already very soon after beam collisions start. Also, exclusive central diffraction can be used for precision measurement of gluon physics.

In looking for the Standard Model (SM) Higgs one should first check the efficiency of the already implemented L1 triggers, for different values of the Higgs mass. LEP gives an experimental lower limit on the mass around 115 GeV from direct searches and indirect electroweak precision measurements at LEP and the TeVatron give an upper mass limit around 300 GeV. In addition, the Higgs is easier to detect for higher masses at the LHC, so the thesis focuses on the detectability of a diffractively produced Higgs near the LEP limit.

This thesis is one in a chain of several theses (Ref. [3] and [4]) investigating different experimental aspects related to the feasibility of measuring a low-mass Higgs at the LHC through diffractive processes.

1.3 Overview of this thesis

The purpose of this thesis is to investigate CMS/TOTEM L1 triggering on diffractively produced Higgs boson events as a function of the accelerator luminosity. Some not yet implemented trigger primitive combinations that could be added at L1 to give appreciable additional efficiency at a reasonable extra background rate are also studied. A full CMS detector simulation is used for generating the L1 trigger primitives. The results of the thesis will be included in the to be published review "Prospects for Diffractive and Forward Physics at the LHC" on the physics of combined CMS and TOTEM data taking.

This thesis is organized as follows: In the rest of this chapter, there is a short introduction to the physics used in this thesis, i.e. the Standard Model and Feynman diagrams, and then the LHC is described. In chapter 2, the theory of the Higgs mechanism is introduced, as well as Higgs production and Higgs decay at the LHC. Chapter 3 presents the software tools used. Chapter 4 contains the results of this thesis, and in Chapter 5 conclusions are drawn. Section 4.1 has been expanded to an internal CMS note, and is given last, in Appendix A.

1.4 Particle physics primer

1.4.1 The Standard Model

The presently accepted model of particle physics is called the Standard Model (SM) and contains three of the four fundamental interactions in nature, namely electromagnetism and the weak and strong nuclear forces, but not gravity. The SM consists of two distinct theories, namely the electroweak theory and Quantum Chromo-Dynamics (QCD, the quantum theory describing the strong force).

According to the Standard Model, there are three generations of matter particles having two quarks and two leptons each, which are all called fermions. Of these, only the first generation is stable.

There are also twelve force carriers for the three forces, namely one for the electromagnetic force, three for the weak force, and eight for the strong force. All fermions in the Standard Model couple to the weak force, while only the charged particles couple to the electromagnetic force, and just the quarks and gluons couple to the strong force.

These force carrier particles are called bosons. The definition of fermions and

Table 1.1: The particles and force carriers in the Standard Model, according to [5] and [6]. $\overline{MS}$ is the most popular renormalization scheme, which is necessary since the quarks are confined inside hadrons and their mass is therefore determined indirectly through their influence on hadronic properties; all other quark masses are also calculated using this scheme, except for the top-quark which decays before it has time to hadronize.

Name	Symbol	Mass	Charge	Spin
Quarks				$\frac{1}{2}$
up	u	1.5-3 MeV/c^2	2/3	
down	d	3-7 MeV/c^2	-1/3	
charm	c	$1.25 \pm 0.09\ GeV/c^2$	2/3	
strange	s	70-120 MeV/c^2	-1/3	
top	t	$174.2 \pm 3.3\ GeV/c^2$	2/3	
bottom	b	$4.20 \pm 0.07\ GeV/c^2$ ($\overline{MS}$)	-1/3	
Leptons				$\frac{1}{2}$
electron	e	511 keV/c^2	-1	
electron neutrino	ν_e	$< 3\ eV/c^2$ (*)	0	
muon	μ	106 MeV/c^2	-1	
muon neutrino	ν_μ	$< 190\ keV/c^2$ (*)	0	
tau lepton	τ	1.78 GeV/c^2	-1	
tau neutrino	ν_τ	$< 18.2\ MeV/c^2$ (*)	0	
Electroweak vector bosons				1
photon	γ	0 eV ($< 6 * 10^{-17}\ eV/c^2$)	0	
W-boson	W^-/W^+	80.40 GeV/c^2	± 1	
Z-boson	Z	91.19 GeV/c^2	0	
gluons (SU(3) colour octet)	g	0 MeV/c^2	0	1
SM scalar boson				0
Undiscovered Higgs	H	$> 115\ GeV/c^2$	0	
(*)	See text	$> 9\ meV/c^2$		

bosons is that a boson has intrinsic quantum mechanical spin $n * \hbar, n = 0, 1, 2, \ldots$ while a fermion has spin$(n + \frac{1}{2}) * \hbar, n = 0, 1, 2, \ldots$. They also differ in that the net number of fermions (number of fermions minus number of antifermions) is always conserved, while bosons can be created in any number.

A further scalar boson for generating the mass of the fundamental particles called the Higgs is as yet undiscovered, the search for it being the topic of this thesis. All these particles are listed in Table 1.1 with their most important characteristics.

The first generation quarks are the constituents of the atomic nucleus, in composite particles called protons and neutrons, while all other combinations of quarks form various unstable hadrons, called baryons when they consist of three quarks, and mesons when they are formed from a quark and an antiquark. Because only quarks and gluons interact with the strong force, they can not be seen as free particles, since the potential between them grows very large at small energy scales, corresponding to large inter-quark distances. This implies that if for example the quark and antiquark of a meson are separated more than some femtometers there will be enough energy to create a quark-antiquark pair between them, confining the original quarks within separate mesons.

The first generation leptons are, respectively, the electron neutrino and the electron. The electron, being a stable charged particle much less massive than a proton or neutron, orbits the atomic nucleus at much larger distances than the nuclear size. This means that chemical reactions of an atom are determined by the electron structure of the atom alone. The neutrino, on the other hand, is a much more elusive particle since it has no electric charge nor does it interact strongly, implying that it only feels the weak force. This force is weak because the masses of the intermediate vector bosons that convey it are very large (80-90 GeV), so that the effective range of the virtual force carriers is of the order of magnitude

$$(\hbar * c)/(80 - 90 \text{ GeV}) = O(10^{-18} \text{ m}).$$

Because this length scale is very much smaller than the size of an atom, the probability of any interaction taking place between a neutrino and any of the pointlike constituents of the atoms is very small. This leads typically to astronomical distances between successive interactions (an average of which is the interaction range) for neutrinos; for example, the neutrinos emitted by the fusion reactions in the sun have an average interaction range in lead of the order of light years. Thus the usual way to identify neutrinos produced in a particle collision is to look for missing energy and

nonconserved total momentum.

In 1998, the Super-Kamiokande Collaboration [6] found that muon neutrinos from the decay of the secondary muons created by cosmic rays in the atmosphere oscillated into some other undetectable flavor (tau neutrino, or a hypothetical sterile neutrino), which could only happen if neutrinos had non-zero mass. Thus, these oscillations take place because the neutrino flavor eigenstates are not equal to the mass eigenstates. The constraints available from this experiment where mainly on the difference between the squares of the two masses $\Delta m_{ij}^2 = |m_i^2 - m_j^2|$. They gave only a lower limit to the masses, if one assumes that one of the neutrinos was massless, but one could not exclude the case of nearly degenerate masses.

In 2001, the heavy water Sudbury Neutrino Observatory (SNO) [7] made observations of the solar neutrino flux of both electron neutrinos and with a lower sensitivity of all flavors. These observations showed that the shortfall of neutrinos with respect to solar models that had already been seen by Ray Davis [8] in 1968 could be satisfactorily explained by another of the neutrino flavors having mass. The best-fit region according to Ref. [5] is $\Delta m_{21}^2 = (8.0^{+0.4}_{-0.3}) * 10^{-5}\, eV^2$ and $\Delta m_{32}^2 = (1.9 - 3) * 10^{-3} eV^2$, meaning that at least two of the three neutrino mass states must have a mass above $\sqrt{\Delta m_{21}^2} \approx 9$ meV.

1.4.2 Diffractive processes

When two protons interact, about 50 % of these interactions are diffractive. In these diffractive interactions the protons lose only a small part of their energy and emerge as protons or low-mass excited baryons. If both leave as protons, the process is called central diffraction in this thesis[1] if a central system is formed between the protons, or elastic scattering if the process is simply $p + p \rightarrow p + p$. If one or both of the protons are excited to a higher-mass state, it is called single or double diffractive dissociation. These diffractive processes are schematically shown in Figure 1.1.

The diffractive processes can be described as an exchange of a pomeron, i.e. an object having the quantum numbers of the vacuum, for fractional proton momentum losses up to a few percent, but for larger losses meson exchanges become important. In QCD this can be described to a first approximation as the exchange of two gluons having combined the quantum numbers of the vacuum, so that there will not be any colour field between the protons.

[1] also known as Double Pomeron Exchange

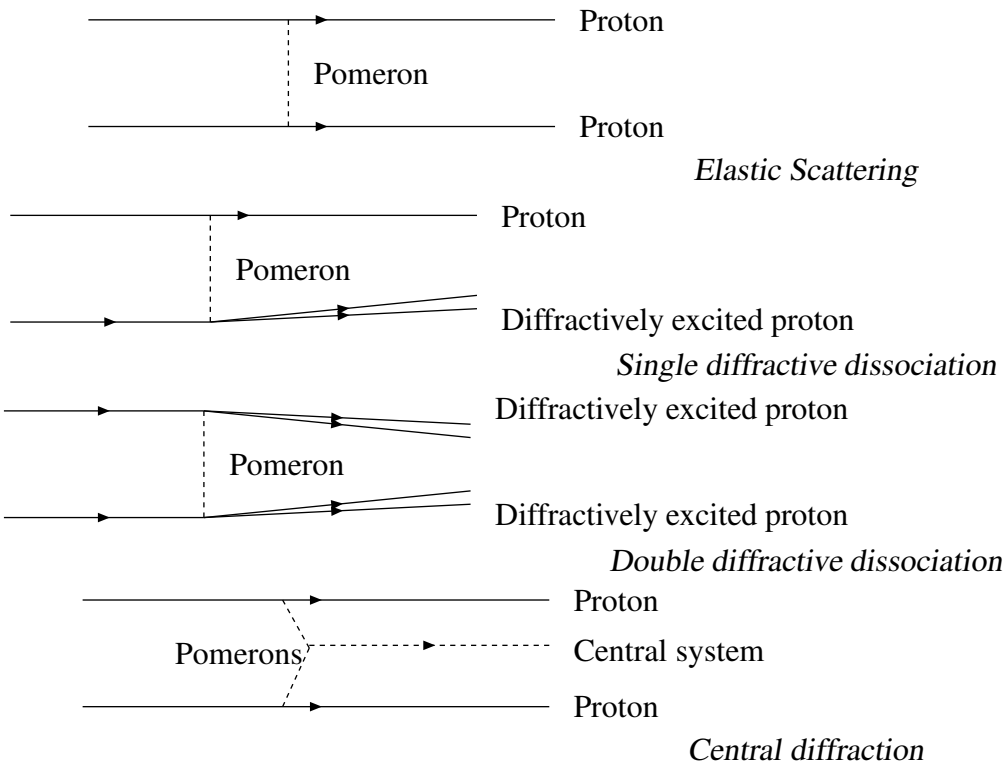

Figure 1.1: Different diffractive processes.

If a central system is produced in the interaction, it will be well separated from the protons in rapidity[2] space. Experimentally this separation is seen as a "rapidity gap", which is a void of any particle production in a certain pseudorapidity[3] interval. However, according to Ref. [9] the exchanged "pomeron" cannot really be considered a particle, since for example in the interaction between a proton and a virtual photon, the photon is absorbed, as viewed in the Breit frame, long before all of the gluons have interacted, forming the "pomeron"-virtual photon scattering process. The Breit frame is also called the "Brick Wall" frame, where the virtual photon has a four-momentum q_γ such that $q_\gamma + 2x_q P = 0$, where x_q is the struck quark momentum fraction and P is the proton four-momentum.

The mass of the central system produced in central diffraction is

$$M^2_{central} \approx \xi_1 \xi_2 s, \tag{1.1}$$

[2]Defined as $y = \ln(\sqrt{\frac{E+p_z}{E-p_z}})$.

[3]defined as $\eta = ln(tan(\frac{\theta}{2}))$, where θ is the polar angle with respect to the beam line. This is $\approx y$, when $p \gg m$ and $\theta \gg \frac{m}{E}$

where ξ is the fractional proton momentum loss and s is the center-of-mass energy squared. The mass can thus be indirectly measured if one can detect both outgoing protons and measure their momenta.

1.4.3 Tests of the Standard Model

The Standard Model has been precisely tested up to energies around 2 Tera-Electron Volts (TeV) in particle accelerators. Some constraints on new physics above that energy are available from precision measurements done at existing accelerators, since some processes that take place unhindered at higher energies still happen with a much lower probability at lower energies. The suppression for some such processes is proportional to the ratio of the collision energy and the mass scale of the new physics raised to some power, while for example the quantum corrections caused by the SM Higgs are proportional to the logarithm of the Higgs mass. More imprecise constraints are available from cosmic ray collisions with atomic nuclei in the atmosphere. Because these are fixed-target collisions, even the highest-energy cosmic ray ever seen, which had an energy around $E_1 = 50$ J = $3.1 * 10^8$ TeV, would only have given a Center-of-Mass (CM) collision energy of $E_{CM} = \sqrt{2 * E_1 * m_p} = 765$ TeV, assuming it collided with a hydrogen atom. A cosmic ray above that energy is at present seen much less often than once per year for even the largest cosmic ray detectors, by definition. Therefore the precision of our data above a few hundred GeV will indeed improve by many orders of magnitude when data from the LHC becomes available.

The accelerators used to test the SM have had almost exponentially growing CM collision energies ever since the first particle accelerators were built at the end of the 1920s. The highest energy tests have been done at the presently running TeVatron collider at Fermilab, outside Chicago and at the Large Electron Positron collider (LEP) at CERN, Geneva, which closed in 2000. Both of these have made substantial contributions to the determination of SM parameters, even though the TeVatron collides protons and anti-protons at an energy of 1.96 TeV, whereas the LEP collided electrons and positrons (anti-electrons) at an energy of less than 0.209 TeV. The reason for this is that the proton is not a pointlike particle, but consists of three valence quarks, plus virtual gluons and sea quarks that bind them together. Therefore the effective collision energy is on the average much less than 1 TeV. In most collisions no valence partons in the different protons interact with each other; only virtual gluons and quarks are struck in at least one of the colliding protons, producing an irreducible low-energy

background. This background was absent from LEP, since the electron is a pointlike particle, and the effective collision energy was thus mostly equal to the CM energy.

1.4.4 Feynman diagrams

In quantum mechanics, the probability of detecting a particle at a position $\vec{x_0}$ is $|\psi(\vec{x_0})|^2$, where ψ is the wave function, or the amplitude for that particle. If one of many identical particles is detected, one must add their amplitudes together before taking the absolute value squared, since the wave functions can interfere with each other. In particle accelerators one is also interested in having some measure of the probability of specific processes. This turns out to be most naturally satisfied by using the concept called a cross section. A cross section is the notional area each particle is assigned to convert a given flux of colliding particles to the measurable rate for the specific process of interest.

The cross-sections σ of all processes in the Standard Model can in principle be calculated by expanding the amplitude ($\sigma \propto |Amplitude|^2$) as a power series in a theory-specific coupling constant which has to be small for the series to converge. The cross section is obtained by adding together the amplitudes of each possible process that takes the specified incoming particles and ends with the specified outgoing particles. These simple particle processes can graphically be presented using Feynman diagrams, which consist of the parts presented in Figure 1.2. The amplitude corresponding to a given diagram is found by multiplying factors for each line and each vertex, and integrating over any internal loops. This power series expansion is also called a perturbative expansion.

Example Feynman rules

As an example, here follow the Feynman rules for calculating the matrix element for electron and photon interactions, from Ref. [10].

First, draw all Feynman diagrams with up to a given number of vertices. They will consist of electron lines, photon lines, and vertices having one incoming and one outgoing electron line and one photon line . Each vertex will contribute a factor

$$(2\pi)^4 * e * (\gamma^\mu)_{\beta\alpha} * \delta^4(k - k' + q),$$

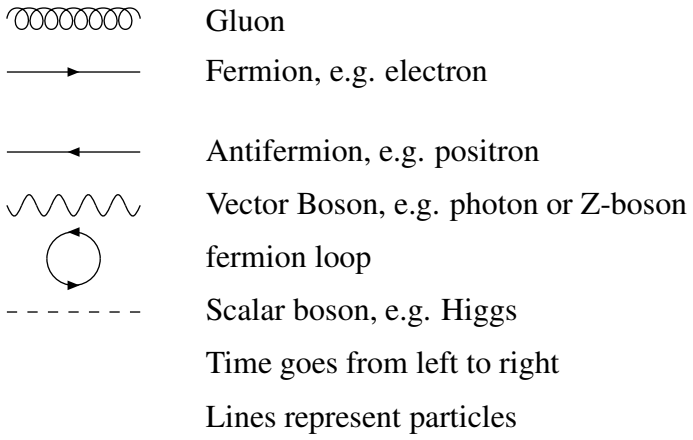

Figure 1.2: Feynman diagram glossary

where e is the electron charge, γ^μ are the gamma matrices,

$$\gamma^0 = \begin{pmatrix} I_{2*2} & 0 \\ 0 & -I_{2*2} \end{pmatrix}, \gamma^i = \begin{pmatrix} 0 & \sigma^i \\ -\sigma^i & 0 \end{pmatrix},$$

$$\sigma^1 = \begin{pmatrix} 0 & 1 \\ 1 & 0 \end{pmatrix}, \sigma^2 = \begin{pmatrix} 0 & -i \\ i & 0 \end{pmatrix} \sigma^3 = \begin{pmatrix} 1 & 0 \\ 0 & -1 \end{pmatrix},$$

and α and β are the gamma matrix index for the incoming and outgoing electron lines, respectively. The δ-function ensures that the sum of the four-momentum of the incoming electron, k, and the photon four-momentum q will be equal to that for the outgoing electron, k'. The four-momentum is a four-vector whose time-component p^0 is the energy, and the other three components form the usual three-space momentum $\vec{p}$. For the initial and final state particles the norm, i.e.

$$p^2 = \sum_\mu p^\mu * p_\mu = \sum_{\mu,\nu} \eta_{\mu\nu} * p^\mu * p^\mu = (p^0)^2 - (\vec{p})^2,$$

is equal to the mass of the particle squared, but internal lines need not fulfill this on-mass-shell condition, as long as the four-momentum is conserved at each vertex. Here $\eta_{\mu\nu} = -I_{4*4} + 2 * \delta_{0\mu} * \delta_{0\nu}$ is the Minkowski spacetime metric of special relativity.

Each external electron line will give a factor $spinor(\vec{p}, \sigma)/(2*\pi)^{3/2}$, where $spinor$ can be $\overline{u}_\beta$ or u_α for an electron in the final or initial state, respectively, whereas for a positron it is v_α or $\overline{v}_\beta$ in the final or initial state, respectively. σ is the z-component of the electron spin. A spinor is a four-component wave function for spin $1/2$ particles,

invented by Paul Dirac. An external photon line contributes a factor

$$e_\mu(\vec{p},\sigma)/\sqrt{(2\pi)^3 * 2p^0}$$

in the initial state, and

$$e^*_\mu(\vec{p},\sigma)/\sqrt{(2\pi)^3 * 2p^0}$$

in the final state. Here e_μ means the photon polarization vector.

Each internal electron line between two vertices, having a four-momentum of k, will include a factor

$$\frac{-i}{(2\pi)^4} * \frac{[-i * \sum_{\nu=0}^{3} \gamma_\nu * k^\nu + m * I_{4*4}]_{\alpha\beta}}{k^2 + m^2 - i * \epsilon},$$

where m is the electron mass, ϵ is infinitesimal, and β labels the vertex the line comes from and α the one it goes to. An internal photon line gives a factor

$$\frac{-i}{(2\pi)^4} * \frac{\eta_{\mu\nu}}{q^2 - i * \epsilon},$$

where q is the photon four-momentum.

Lastly one integrates the product of all these factors for each diagram over all internal momenta, and sums over all Dirac ($\alpha, \ldots$) and spacetime ($\mu, \ldots$) indices, and adds together the results for all diagrams.

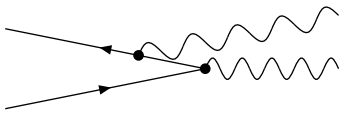

Figure 1.3: Example Feynman diagram with two vertices, one internal electron line, two external electron lines and two two external photon lines. A diagram with only one vertex, i.e. $e^+ + e^- \rightarrow \gamma$ would not work since in the center-of-mass frame the momentum of the photon would have to be equal to zero while the energy would be larger than $2m_e c^2$.

Thus one can calculate using these rules, for example, the electron-positron annihilation cross section, i.e. the reaction $e^+ + e^- \rightarrow \gamma + \gamma$. The tree-level diagram, i.e. the one without any internal loops, for this process is shown in Figure 1.3.

Even when looking at diagrams with just a few loops, there will still be quite a lot of possible permutations of the loops, but the first term, i.e. the one with no loops,

is still dominant for almost all processes that are allowed without any internal loops; the dominant Feynman diagrams for electroweak processes disallowed at tree-level are called penguin diagrams. The first term often gives the largest contribution since the electromagnetic coupling constant is $\alpha_{(EM)} \approx 1/137$ at low energy scales and grows logarithmically with energy, not exceeding 0.01 at any reachable energy.

In practice, because the weak and electromagnetic coupling constants are small at all accessible energies, this perturbative expansion works well for them, whereas the previously mentioned low-energy imprisonment of the quarks is caused by the growth of the strong force coupling constant from 0.119 at the mass of the Z-boson to unity at an energy scale of a few hundred MeV. Below approximately 1 GeV, perturbation theory calculations thus don't converge quickly enough if at all for QCD. Here one must thus come up with some ad hoc model validated by low-energy experiment, like Regge-theory [11].

One reason for using these Feynman diagrams instead of just making all the various integrals and calculations one by one without this graphical aid, is that the Feynman diagram method uses unchanging rules for each diagram, whereas if one just did ad hoc calculations, unnecessary further scope for errors would be introduced.

1.5 LEP and the LHC

CERN (Conseil Européen pour la Recherche Nucléaire) is a large European particle physics center at the French-Swiss border in Geneva, whose flagship particle accelerator during the last two decades was the Large Electron-Positron (LEP) collider, which was housed in an underground circular tunnel having a circumference of about 27 km.

The Large Hadron Collider (LHC) was proposed as a hadron collider that would reuse the LEP tunnel. It was first mooted in the 1980s. To compete with the U.S. Superconducting Supercollider (SSC) it was decided to maximize the luminosity of the LHC to compensate for the lower energy of the LHC compared to the SSC, which was due to the LHC having a shorter tunnel. By using proton-proton collisions, the constraints and inefficiencies from antiproton production, deceleration, storage, and reacceleration that had plagued among others the TeVatron, would also be relieved. Of course, this advantage was bought at the cost of making the dipole magnets more complicated, because the counterrotating beams could not go through the same vacuum pipe. This is in contrast to the case of proton and antiproton beams which could share

a common vacuum pipe, having opposite charges going opposite ways.

During 1999-2000, the LEP center-of-mass energy was raised as high as it could go in the search for the Higgs boson and any other heavy particles predicted by extensions of the Standard Model; from the Z-production peak at $M_Z = 91$ GeV to 209 GeV near the end. The most acute limit on the collision energy at the end was synchrotron radiation from the electrons, which cause energy losses at a rate proportional to the electron energy to the fourth power. Thus even if one found a way to double the amount of energy being used to accelerate the leptons, that would still only raise the collision energy by $\approx 20\%$.

Just at the end, in November 2000, two of the experiments at LEP had found a 3-σ signal from a putative 115 GeV/c^2-mass Higgs, and thus all four experiments asked for an extension into 2001 of the data taking, which was not granted to expedite LHC construction. The majority of the LHC construction consisted of removing the old LEP detectors, magnets and beam vacuum vessel and installing the new ones instead, plus other necessary beam infrastructure.

The protons in the LHC will first be accelerated in the Super Proton Synchrotron (SPS) to 450 GeV and then injected into the main ring in the form of bunches containing $\sim 10^{11}$ protons each, the bunch separation being 25 ns, corresponding to a distance of 7.5 m. They are then accelerated to 7 TeV, for a center-of-mass collision energy of 14 TeV when they collide almost head-on; the crossing angle is not precisely zero so that the beams separate after the designated interaction point (IP). However, even when the beams are compressed to their minimum cross section of $\sim 20\ \mu m$ only a few of the protons experience high-energy scattering, since the effective proton radius is ~ 1 fm.

The present timetable for the LHC turn-on is that all the detectors will be installed during 2007 and that there will be colliding beams around the end of 2007, with an intention of reaching the design luminosity, $10^{34}\ cm^{-2}s^{-1}$, as soon as possible (within three to five years from turn-on).

For an overview of the main LHC parameters, see Table 1.2.

1.6 LHC experiments and triggers

The four main interaction points of the LHC house, respectively, the all-purpose experiments ATLAS and CMS (the forward physics experiment TOTEM is housed around

Table 1.2: Parameters of the Large Hadron Collider at CERN [12], taken from Ref. [13]

	Injection	Collision	Collision
Parameter [unit]		Design	Stage 2 Commissioning
Luminosity $[cm^{-2}s^{-1}]$	-	$1.0 * 10^{34}$	$5. * 10^{32}$
Bunch crossing frequency [ns]	25	25	75
Number of bunches	2808	2808	936
Circulating beam current [A]	0.582	0.582	10^{-3}
Protons per bunch	$1.15 * 10^{11}$	$1.15 * 10^{11}$	$6 * 10^{10}$
Interactions per crossing	-	19.3	2.9
Proton energy [GeV]	450	7000	7000
Stored energy per beam [MJ]	23.3	362	63

the CMS interaction point, at distances from 10 m to 220 m), the heavy-ion experiment ALICE, and the bottom-quark experiment LHCb. Of these, this thesis will concentrate on the combined data taking of the CMS and TOTEM experiments.

The CMS [14] interaction point is surrounded by a large superconducting dipole magnet which creates a very intense 4 T magnetic field throughout its interior for easy muon momentum measurement without needing to have an unprecedentedly good muon chamber resolution. The diameter of the central cylindrical cavity through the dipole magnet is 5.9 m, and this cavity contains, in addition to the beam vacuum vessels and the IP, several detectors. One of these is the silicon Inner Tracker which consists of three layers of silicon pixel detectors nearest to the IP having a total area of $\sim 1\ m^2$, and ten layers of silicon microstrip detectors beyond them having a total area of 200 m^2. The Inner Tracker has particle tracking capability up to pseudorapidities [4] $\eta = \pm 2.4$, corresponding to particles leaving the IP at an angle larger than ten degrees. This detector can resolve the common vertex of the decay products of heavy-quark hadrons that decay relatively far from the IP (more than a few tens of micrometers away). It is also able to measure the momentum of the charged particles since the detector is permeated by a 4 T magnetic dipole field.

After this precision detector comes the electromagnetic calorimeter (ECAL), which

[4] defined as $\eta = ln(tan(\frac{\theta}{2}))$, where θ is the polar angle with respect to the beam line. This is $\approx y$, when $p \gg m$ and $\theta \gg \frac{1}{\gamma}$

consists of 61200 lead tungstate ($PbWO_4$) scintillating crystals, and photodetectors to convert the resulting light into electrical signals. This detector intercepts electrons and photons up to $|\eta| = 3$, but can't stop heavier particles.

The long-lived heavy particles, i.e. muons and hadrons, go on to the hadronic calorimeter (HCAL), which is the outermost detector inside the dipole magnet, and also has some scintillators on the outside of the magnetic coil. To maximise the absorption within the central cavity most of the space beyond the ECAL is filled with brass, the embedded detector volume being minimized by using plastic scintillator tiles connected by long optical fibers to photodetectors outside the cavity. The HCAL detects hadrons up to $|\eta| = 5$.

Finally, muons are caught by the muon chambers, but neutrinos (and other hypothetical stable very weakly interacting particles) escape undetected. There are three different muon detectors: Drift Chambers in the central region ($|\eta| < 1.2$) where muon rates, the residual magnetic field and the neutron induced background are low; Cathode Strip Chambers in the endcap ($1.0 < |\eta| < 2.4$) where all these are higher, and Resistive Plate Chambers in both regions ($|\eta| < 2.1$) that can stand very high muon rates and provide a fast signal for triggering.

The TOTEM collaboration has two near forward telescopes for charged particle tracking, one at 7.5-10.5 m and the other at 14 m from the IP, covering pseudorapidities of $3 < |\eta| < 5$ and $5.3 < |\eta| < 6.6$ respectively. There are also very forward roman pot detectors at 147 m and 220 m from the interaction point. The implementation of detectors at 420 m from the IP is being studied; see Ref. [15]. The very forward detectors are used to detect the scattered protons that have lost at most a few percent of their original beam momentum.

Chapter 2

The Higgs boson

The pioneers of relativistic quantum theory for electromagnetism (QED), among others Richard Feynman, found that certain calculations with the by assumption pointlike elementary particles would give a result of infinity, which is obviously non-physical. Later, it was found that one could add a finite number of corrections that absorbed the infinities (the procedure was called renormalization). There were just a few of these corrections in QED, and by using them one got a mathematically somewhat non-rigorous theory that worked, and gave correct results with a precision better than one part per billion (see for example Ref. [16]). However, when one tried to manually add mass terms to the Standard Model Lagrangian, which parametrizes all interactions in the model, it was found that the resulting theory was non-renormalizable. Therefore, some other way to add the observed masses had to be found.

The Higgs mechanism for mass generation was invented by Peter Higgs in 1964 [17], and consists of adding spontaneous symmetry breaking to the model. The simplest model for which this is possible, has a complex scalar field ϕ, with a Lagrangian (which is by definition equal to a kinetic energy term T minus a potential energy term V)

$$\mathscr{L} = T - V = \frac{1}{2}(\partial_\mu \phi)^*(\partial^\mu \phi) - (\frac{\mu^2}{2}\phi^*\phi + \frac{\lambda}{4}(\phi^*\phi)^2)$$

This consists of kinetic, mass and quartic self-interaction terms. If μ^2 is positive, the potential term will have a minimum at $\phi = 0$, but if it is negative the minimum is all points on a circle with radius $|\phi|_0 = v = \sqrt{-\mu^2/\lambda}$. The absolute phase of the minimum being irrelevant, one may set it to zero and expand ϕ around this value $\phi = v+\eta+i\xi$, where both η and ξ are real scalar fields and v is the vacuum expectation

value of the Higgs field, giving a new Lagrangian

$$\mathscr{L} = \frac{1}{2}(\partial_\mu \eta)^2 - \lambda v^2 \eta^2 + \frac{1}{2}(\partial_\mu \xi)^2 - \lambda(v\eta^3 + \frac{1}{4}\eta^4 + \frac{1}{4}\xi^4 + v\eta\xi^2 + \frac{1}{2}\eta^2\xi^2) + \frac{1}{4}\lambda v^4.$$

Now we have a massive (η, mass $= \sqrt{-2\mu^2}$) and a massless (ξ) real scalar. The massless scalar is a Goldstone boson [18] and cannot be a real particle, since no such particle has been observed. This particle can be removed by making the Lagrangian locally gauge invariant, meaning that it should be invariant under a change

$$\psi' = U(x_\beta)\psi = e^{i\alpha(x_\beta)Q}\psi,$$

where Q is the charge and $\alpha(x_\beta)$ is a function of the space-time coordinate x_β. Only the kinetic term need be changed, and this is most easily done by adding a massless vector field A^μ and replacing partial derivatives by covariant derivatives defined as

$$D^\mu = \partial^\mu - iA^\mu Q.$$

If the field transforms locally like

$$A'_\mu = A_\mu + \partial_\mu \alpha(x)$$

and a kinetic term for this field is added to the Lagrangian

$$\mathscr{L} = \frac{1}{2}(D_\mu \phi)^*(D^\mu \phi) - (\frac{\mu^2}{2}\phi^*\phi + \frac{\lambda}{4}(\phi^*\phi)^2) - \frac{1}{4}F_{\mu\nu}F^{\mu\nu},$$

it will then be locally gauge invariant. Here, too, a mass term would break local gauge symmetry. However, since α is a function of the same spacetime coordinates x_β as ϕ, one can fix a particular gauge by choosing $\alpha(x) = -arg(\phi(x))/q_\phi$, making ϕ real in this gauge. This gets rid of the Goldstone boson, since the theory should be invariant under gauge transformations, and for one particular choice of gauge, the Goldstone boson has no physical existence. Thus by setting $\phi = v + h(x)$, one gets a Lagrangian

$$\mathscr{L} = \frac{1}{2}(\partial_\mu h)^2 + \mu^2 h^2 - \frac{1}{4}F_{\mu\nu}F^{\mu\nu} + \frac{q^2}{2}v^2 A^\mu A_\mu - \lambda v h^3 - \frac{\lambda}{4}h^4 + q^2 v A^\mu A_\mu h + \frac{q^2}{2}v A^\mu A_\mu h^2$$

The first two terms define a massive real scalar (the Higgs), the second two a massive gauge boson, and the rest are interaction terms.

This is certainly an elegant mass generation scheme, but to prove that it really is true, we will have to discover the scalar Higgs boson, and ideally also measure many of

its properties, like mass, self-coupling, quantum numbers and width, since they should not all be independent.

Furthermore, because the self-interaction gets larger for larger Higgs masses, there is an upper bound in the SM on the mass of the Higgs, beyond which this self-interaction would violate unitarity. This maximum SM mass is of the order 1 TeV, meaning that the LHC should be able to find or exclude the SM Higgs at all possible masses.

2.1 Higgs production

The Higgs production cross section in any particular production process is intimately connected to the corresponding Higgs partial decay width since the process $H \leftrightarrow particles$ can happen in either direction. The Higgs particle couples to fermions with a coupling constant $g_{f\overline{f}H} = m_f/v$, where v is the vacuum expectation value of the Higgs field, whereas for the weak gauge bosons $W^{\pm}$ and Z^0 it couples like $g_{W^+W^-H} = 2m_W^2/v$ and $g_{ZZH} = 2m_Z^2/v$ [19]. The partial decay width of the Higgs to a fermion-antifermion pair is proportional to this coupling constant squared. Therefore the Higgs production cross section is dominated by processes where the Higgs couples to the most massive particles, namely the top quark and the weak gauge bosons. For example, the dominant mode of Higgs production at both the LHC and the TeVatron colliders is gluon-gluon fusion with an internal top loop coupling to the Higgs. See Figure 2.1 for Feynman diagrams of the direct Higgs production processes in a hadron collider, and Figure 2.2 for the cross sections of these processes at the LHC as function of the Higgs mass, calculated within the Standard Model in Ref. [20].

2.2 Higgs decay

The Higgs will preferentially decay to the highest mass fermions having a mass less than half the Higgs mass, but because of differences in the other factors in the decay amplitudes to fermions and gauge bosons, it turns out that below a Higgs mass of 140 GeV the decay to $b\overline{b}$ is dominant, whereas above that W^+W^- dominates. See Figure 2.3 for branching ratios and Figure 2.4 for total decay width, both figures taken from Ref. [23]. The W^+W^- dominance is caused by the partial decay width to W^+W^- being twice that for ZZ at large Higgs masses where the Higgs-vector boson coupling

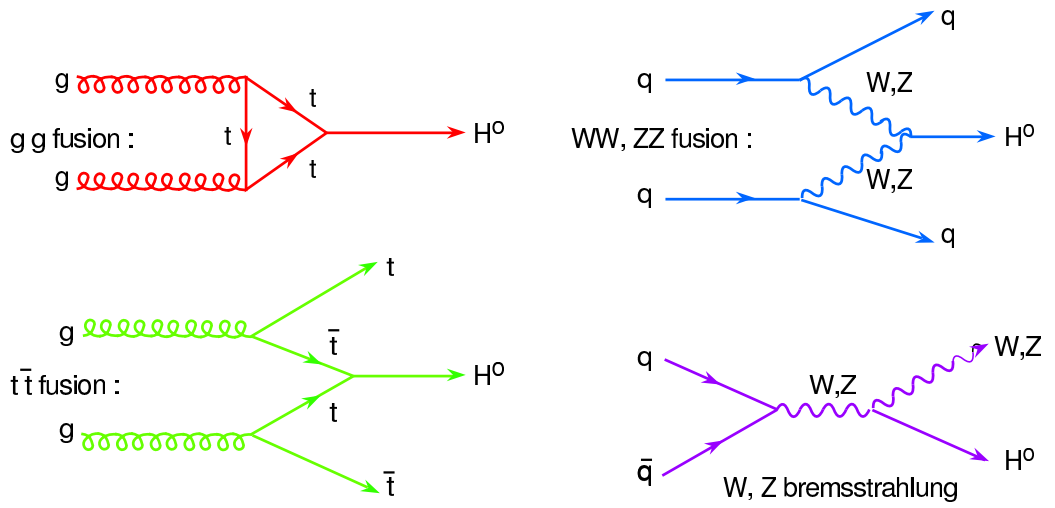

Figure 2.1: Higgs production Feynman diagrams at hadron colliders, from Ref. [22]

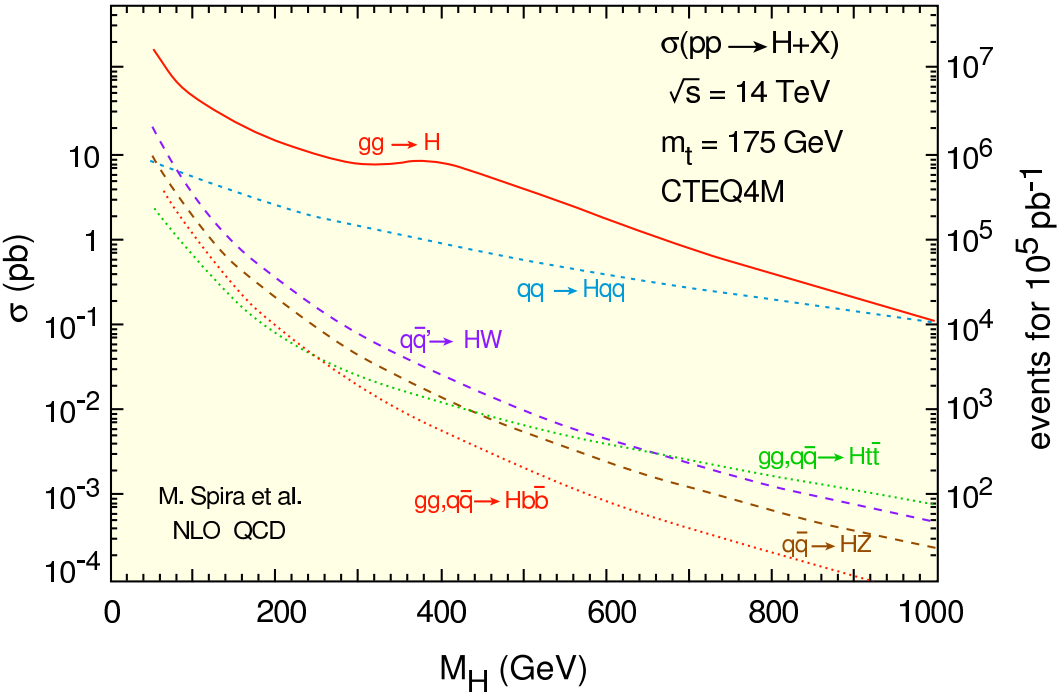

Figure 2.2: Higgs production cross sections at the LHC, from Ref. [20]

is strong, as calculated by Ref. [21]. Also, when both W-bosons are real, around $M_H \approx 2M_W$, $\Gamma(ZZ^*)$ is reduced to just 2 % of $\Gamma(W^+W^-)$. Lastly, even for a very massive Higgs above 400 GeV, the top-antitop branching ratio never exceeds either of the vector boson branching ratios.

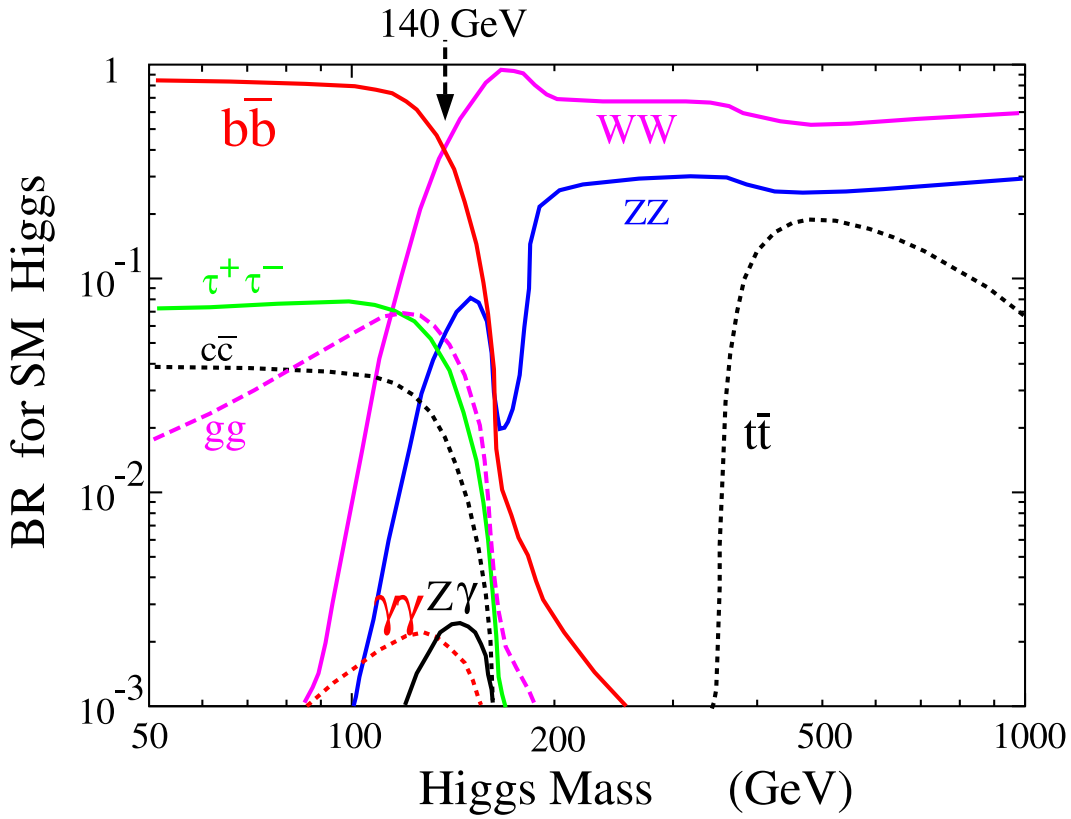

Figure 2.3: Branching ratio of various Higgs decay modes, as a function of Higgs mass, from Ref. [23]

2.3 Pre-LHC Higgs searches

The most far-reaching pre-LHC Higgs search was done at LEP, where a 95% confidence lower mass limit of 115 GeV was found. The corresponding limits set by the TeVatron are even lower, in spite of the higher beam energy and total integrated luminosity, because of the higher backgrounds and larger dispersion in collision energy values and measured jet energy.

At Fermilab, a SM Higgs can be detected at 3-5σ statistical significance only up to a mass of 130-140 GeV, depending on the expected integrated luminosity collected by the planned shutdown of the TeVatron at the end of 2009.

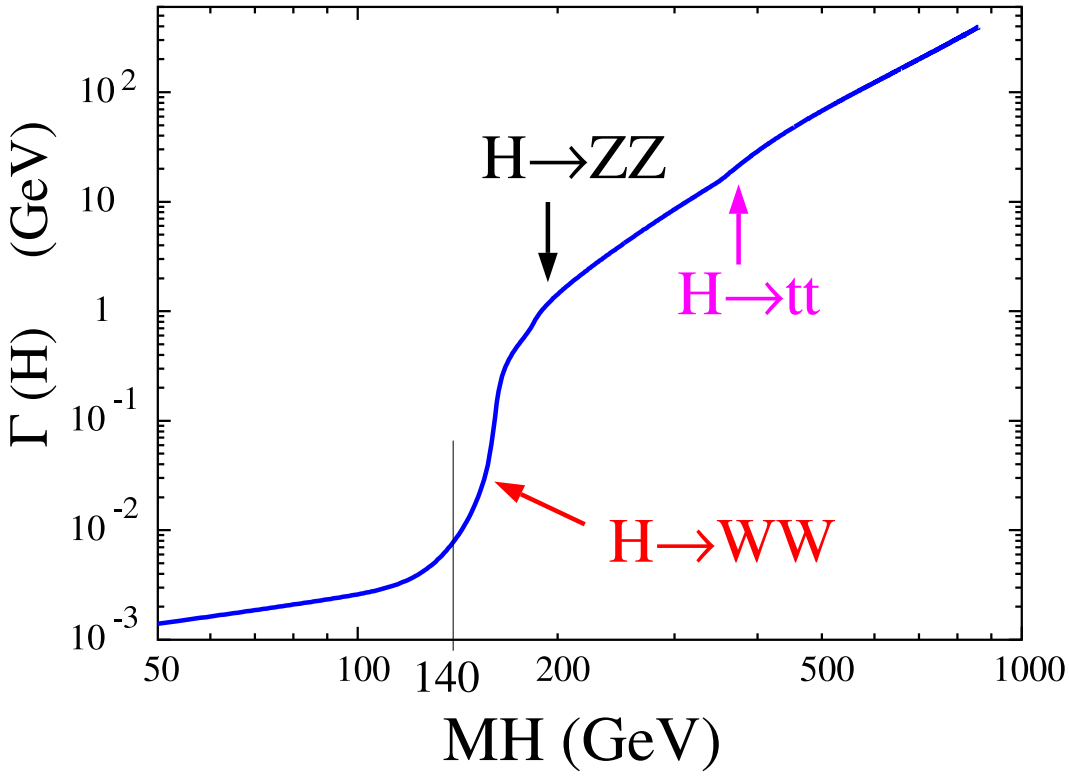

Figure 2.4: Decay width of SM Higgs, as a function of Higgs mass, from Ref. [23]

2.4 Higgs search at the LHC

The LHC has enough luminosity at high enough collision energy that the total rate of Higgs production is more than one per day at the design collision rate. However, each trigger level must retain an appreciable fraction of the events while at the same time reducing the recorded data rate by many orders of magnitude: at level one the input rate of collisions is 40 MHz and the output rate is 100 kHz, while the post-triggers rate is O(100) Hz. At the same time, a low-mass Higgs decays to a few low-energy jets, which is not distinctive enough from the overwhelming jet background for the decay products to form an unambiguous trigger. Therefore one has to choose triggerable subprocesses, like for example top-antitop-associated Higgs production, which can have up to three additional high-p_T jets per top quark, and also high-p_T leptons. Another highly visible mode is Higgs decaying to two photons, which happens with a branching ratio of $1 - 3 * 10^{-3}$ for a Higgs mass below 150 GeV as can be seen in Figure 2.3. The total Higgs production cross section at the LHC will be dominated by gluon fusion ($g + g \rightarrow H$) and is a decreasing function of the Higgs mass [20], from $\approx$ 30 fb at the

LEP lower limit at 115 GeV to ≈ 10 fb at around 300 GeV, which is the indirect upper limit obtained from precision measurements at LEP using the top mass determined directly by TeVatron as a constraint [24].

2.5 Diffractive Higgs-production

A distinctive mode of Higgs production is central diffractive Higgs production, $p + p \to p + rap.gap + H + rap.gap + p$. Here $rap.gap$ means that, except for possible pileup events, i.e. multiple protons interacting during the same bunch crossing, the very forward protons and the Higgs should be separated by many units of rapidity with no other particles between them. The Higgs is produced with a central pseudorapidity distribution with a width of less than 3 units in rapidity. The protons, on the other hand, are at pseudorapidities $|\eta| > 7$, since they lose only around 1% of their momentum, because the mass of the produced central system is

$$M^2_{Higgs} \approx \xi_1 \xi_2 s,$$

where ξ is the fractional proton momentum loss and s is the center-of-mass energy squared, i.e. (14 TeV)^2 at the LHC.

Thus, if one can measure both forward protons accurately one gets a much better mass resolution for the central system, making for both a more precise measurement of the Higgs mass and a sharp reduction of the background. In Ref. [25] the mass resolution using only the forward protons was studied and found to be O(1) GeV. In addition, one can measure the parity of the central system. Central diffractive production will mostly produce central systems having quantum numbers $J^{PC} = 0^{++}$, according to for example Ref. [26]. Here J is the total angular momentum, P the (spacetime) parity[1] and C the charge conjugation parity[2]. This reduces the $q\overline{q}$ background substantially.

The cross section of this process is quite a bit smaller than the total Higgs production cross section, and was historically also uncertain by orders of magnitude. Lately the predictions fall within an order of magnitude centered on ~ 3 fb [27]. This would give an appreciable sample of Higgs particles after a few year of LHC running, when the LHC creates $O(100)$ fb^{-1} of integrated luminosity per year. This process is a very interesting challenge at L1 even so, since the above-mentioned small cross section

[1] $\vec{x} \to -\vec{x}$

[2] Charge$\to$ $-$Charge

means one has to have a good signal efficiency at L1 without in most cases having any information from the forward proton detectors, because of their distance from the IP and the corresponding signal delays.

A Feynman diagram of the process is shown below in Figure 2.5, and an example of the predictions for the cross section in Figure 2.6.

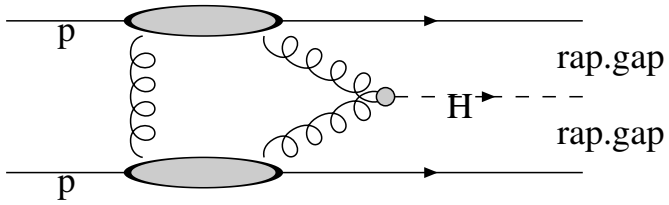

Figure 2.5: Feynman diagram of diffractive Higgs production at LHC

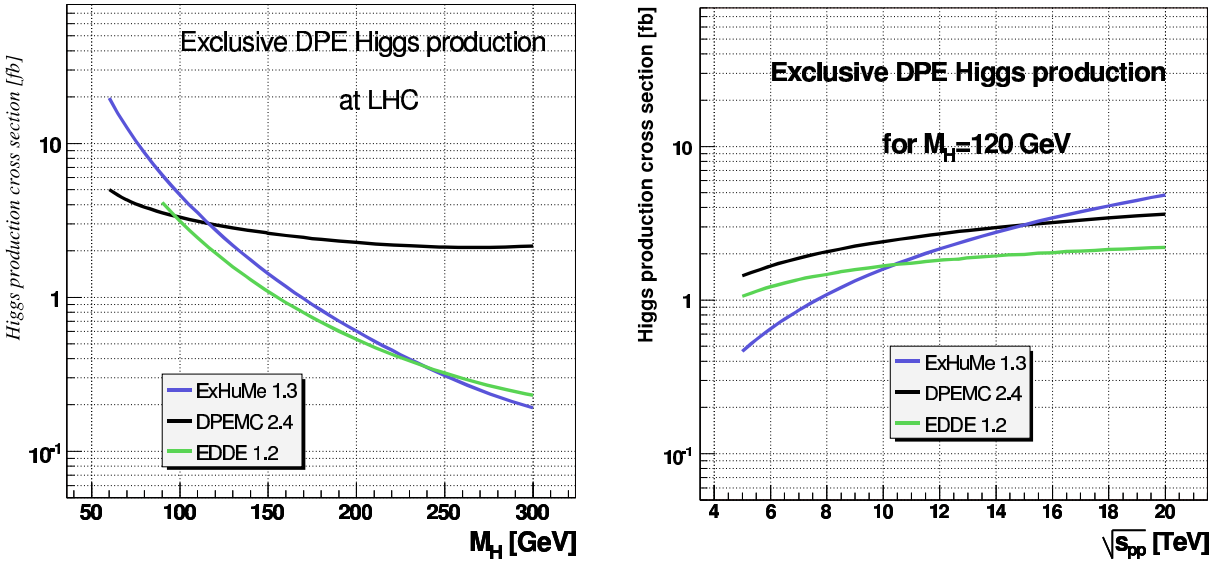

Figure 2.6: As an example, predicted Higgs cross section as a function of Higgs mass and collision energy for three different generators for central diffractive Higgs production, from Ref. [28].

Chapter 3

Tools

3.1 CMS/TOTEM L1 trigger

The CMS/TOTEM L1 trigger is hardware-based, with a few adjustable thresholds and parameters, but the combinations of L1 trigger objects comprising the subset of modes actually triggered on are set before any data is taken and after that they are rarely changed. Thus it is imperative to do simulations beforehand to find as many as possible of the simplest L1 trigger combinations that are reasonably efficient for the particle process of interest while stringently cutting the uninteresting background. The L1 trigger must check all the trigger combinations before the event under study drops off the end of the 128-event queue, so within $128 * 25$ ns = 3.2 μs. At L1, the information from the central system is coarse-grained and no information is available from the very forward detectors beyond 220 m from the IP that have a combined particle plus signal travel time larger than the L1 latency time of $3.2\mu s$.

Of the CMS detectors, only the information from the electromagnetic and hadronic calorimeters and the muon detectors are available at L1.

At L1, jets are reconstructed using the calorimeter response by dividing the complete calorimetry coverage into $22 * 18$ regions in the (η, ϕ)-plane[1]. This aggregates $4 * 4$ calorimeter towers into one L1 calorimeter region (coarsening the resolution by a factor four in both ϕ and η). Then a $3 * 3$ calorimeter region window is slid across the (η, ϕ)-plane, and a new jet is declared to be the $3 * 3$ calorimeter region window with the largest E_T sum such that the central region in the $3 * 3$ window has a larger

[1] $\eta \equiv -\ln(\tan(\theta/2))$ and θ (ϕ) is the polar (azimuthal) angle with respect to the direction of the clockwise turning beam.

E_T than any of its neighbours. The E_T of the jet is set to equal to the E_T sum of the regions in the $3 * 3$ window and its coordinates equal to those of the central region. Since no weighted average is computed, this further degrades the angular localization of the jet. The used regions are then zeroed and the next jet is iteratively searched for using the same algorithm until all jets above a 5 GeV threshold are found. See Figure 3.1 for a visualization of the L1 jet finding algorithm.

On the average this algorithm captures only around 60% of the actual jet E_T, and of course it also degrades the information on the angular localization of the jet. For more on this algorithm and a description of the previous L1 jet calibration that served as a basis for the one used in this thesis, see for example [29].

The muon trigger aggregates the information from three types of muon detectors: the Resistive Plate Chambers (RPC; $|\eta| < 2.1$) which have excellent time resolution and are used for triggering so that any muon can be reliably associated with a specific IP crossing time. The second type of muon detector are Drift Tubes (DT) in the barrel of the CMS detector ($|\eta| < 1.2$) and last are Cathode Strip Chambers (CSC) within the endcap of the barrel ($1.0 < |\eta| < 2.4$). Both of the latter have very good position resolution.

The CSC and DT each have a Local Trigger that finds good track segments and sends them to the two Regional Muon Triggers covering $|\eta| < 1.0$ and $|\eta| > 1.0$, since the CSC and DT detectors overlap. Each of these Regional Muon Triggers sends its best four muon candidates to the Global Muon Trigger. In contrast, the RPC uses a Pattern Comparator Trigger to directly find the best 4+4 muon candidates in the endcap and barrel. Because the CSC and DT-detectors have very good background rejection, whereas the RPC detectors are very efficient, the Global Muon Trigger outputs the four best muons that are either seen by both kinds of detectors regardless of their quality, or that are seen by one of them and have a high quality.

3.2 Simulation

The data used for the results of the thesis were produced on a computing cluster at the University of Wisconsin. The simulation was done by using on the one hand the Monte Carlo particle generator PYTHIA [30] (latest version 6.3) for background (QCD) event samples, and on the other hand the generators EDDE [31] version 1.1 and ExHuME [32] version 1.0 for simulating Higgs production. All three were fol-

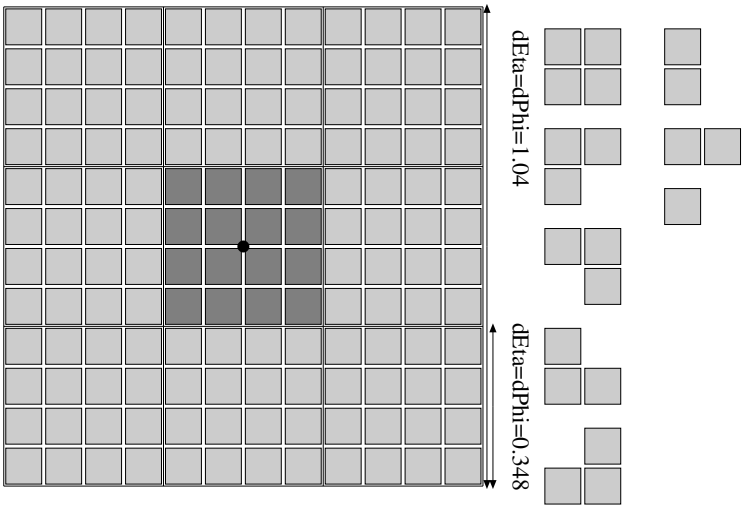

HCAL/ECAL L1 jet finding: in non-central regions the towers are larger in $(d\phi, d\eta)$

Figure 3.1: Visualisation of the L1 jet finding algorithm. Tau-like tower patterns on the right: Tau veto bit not set for each $4 * 4$ region if that region has only four or less contiguous active trigger towers, matching the veto patters shown. To consider an L1 jet a τ jet, none of the nine regions must have a tau veto bit set.

lowed by a detector simulator, which was OSCAR [33], and the reconstruction program ORCA [34].

The analysis was done by running ROOT [35] scripts on the L1 output from the simulation.

3.3 Generators for diffractive Higgs

The diffractive Higgs events were produced using the Monte Carlo event generators EDDE and ExHuME [28]. ExHuME is based on the perturbative calculations of Khoze et al. [1] and adds a soft-survival probability parameter S^2 to capture the nonperturbative low-energy filling-in of the rapidity gaps. EDDE, on the other hand, uses nonperturbative improved Regge-eikonal calculations with Pomeron exchange between the protons without an explicit S^2 parameter, since Regge theory is presumed to implicitly correct for that. To not create any pre-final-state gluons in the rapidity gaps, a Sudakov factor is included in both simulations, making the cross section drop rapidly for larger Higgs masses as the gluon phase space grows. Both of the generators then let PYTHIA evolve their parton-level output to the final hadron-level state. According

to Ref. [28], the total cross sections for a 120 GeV Higgs predicted by EDDE and ExHuME are 1.94 fb and 2.8 fb respectively. Furthermore the rapidity distribution for ExHuME is narrower, thus resulting in a considerably higher detected cross section and efficiency for ExHuME than for EDDE in this channel. The output of both simulations were used, except sometimes when it was previously verified that in that particular case it made no appreciable difference.

Chapter 4

Results

4.1 Jet E_T calibration

For a more detailed treatment of this topic, see appendix A.

At L1 the rough algorithms that are used for the very time-limited jet finding, reconstruct on the average only 60 % of the input jet E_T (see Figure 4.1), varying also as function of the pseudorapidity and the E_T of the jet. Thus, a calibration to remove as much as possible of the variation is necessary, since there is some nonlinearity in the detector response, especially at the lowest detectable energies. These nonlinearities are of concern for detecting a low-mass Higgs, since the maximum jet E_T from its decay is around 60 GeV. In addition, the rate of occurrence of fake jets in the calorimeters with an E_T below 30-40 GeV (corrected) is not precisely known before the LHC is actually running rendering these low energies unusable for triggering for the time being.

The QCD background samples were simulated at the University of Wisconsin Tier-2 computing cluster [1] with PYTHIA version 6.3. A jet-finding algorithm was applied on the final state particles of the events, giving a list of so-called generator-level jets. The events were further run through an OSCAR 2.4.5 full CMS detector simulation and an ORCA 7.6.1 L1 jet reconstruction simulation, giving the reconstructed L1 jets.

The calibration was done by first correlating L1 jets and generated jets. The criteria was that they were within an angular distance of

$$\sqrt{\Delta\eta^2 + \Delta\phi^2} < 0.3(central) \quad or \quad 0.5(forward),$$

where η is the pseudorapidity, and ϕ is the angle of the jet in the plane transverse to the beam. Central jets are the ones with $|\eta| < 3$ and forward jets the ones with $3 < |\eta| < 5$.

[1] www home-page: http://www.hep.wisc.edu/cgi-bin/cms/CMSJug.cgi?p=datasets

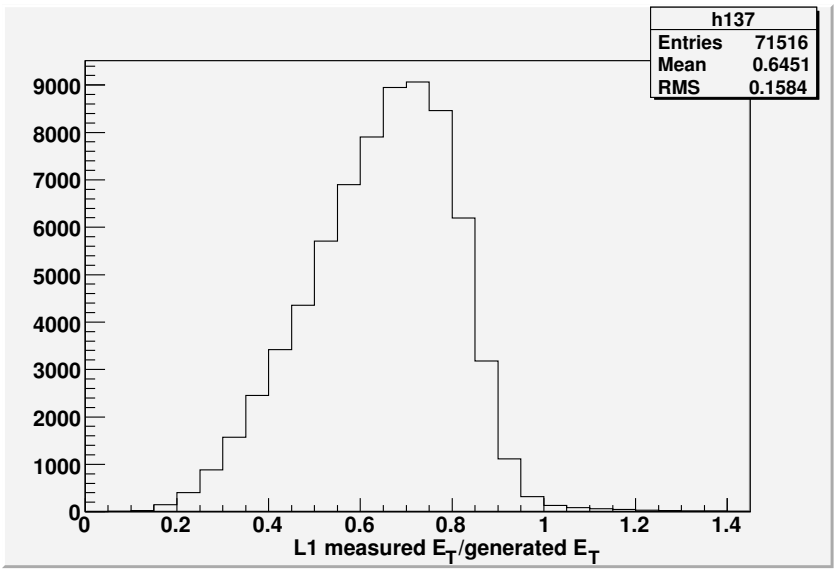

Figure 4.1: L1 measured E_T divided by generated E_T, for jets with a generated $E_T > 50\ GeV$

Each L1 jet was correlated with the closest generated jet fulfilling the above angular distance criterion; if no generated jet was close enough, there was no match, but no check was done to exclude the possibility of multiple L1 jets being correlated with the same generated jet. This was presumed not to be a big problem since the smallest difference in L1 jet angles is a multiple of 0.35 in ϕ, and η for central jets, whereas the corresponding step size for forward jet η is 0.55.

Afterwards, the correlated jets were assigned to one of 22 pseudorapidity bins based on its L1 η, and the generated jet E_T and L1 jet E_T were added to a two-dimensional histogram corresponding to that η-range. All 22 histograms were then fitted with a function consisting of two connected parabolas including the transition point as a fitted parameter also, giving five parameters in all.

However, not to bias the result through misidentification of very low E_T generated jets with unrelated L1 jets, the function was fitted so that it gave the best-fit L1 E_T corresponding to a given generated E_T, while what is wanted is of course the inverse of the function. The decision to use two parabolas was taken since it gave a lower χ^2 and a better fit than any of the algebraically invertible polynomials, i.e. a single polynomial of first, second, third or fourth degree. As stated above, the rapidity binning was approximately 0.3 within the central six units in pseudorapidity and outside that 0.6.

The calibration was found to work well since, as seen in Figure 4.2, the calibrated

L1 E_T is found to be an almost unbiased estimator of the true generated E_T. From Figure 4.4 the post-calibration E_T resolution is found to be

$$\sigma(E_T)/E_T = p0 \oplus p0 * \sqrt{p1} = (6.37 \pm 0.06)\% \oplus (141 \pm 2)\%/\sqrt{E_T[\text{GeV}]}.$$

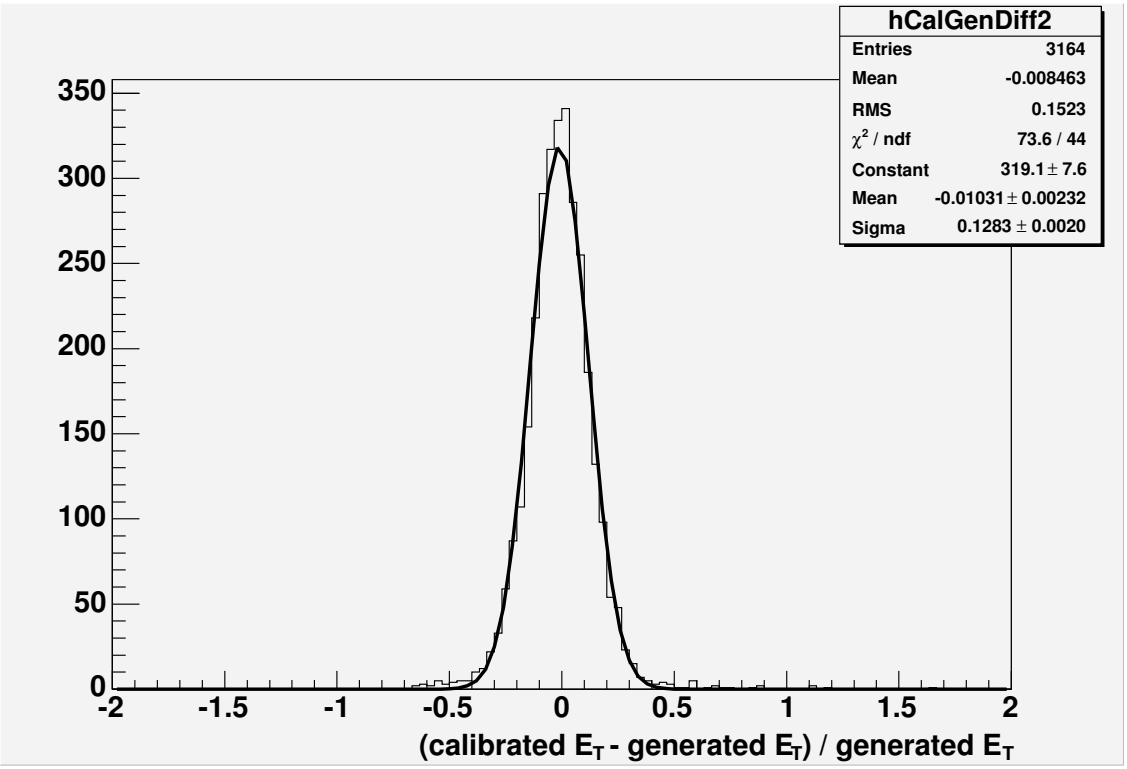

Figure 4.2: Fractional deviation of the corrected E_T from the generated E_T for an independent QCD sample. E_T was required to be within the domain of validity of the calibration fit. QCD sample 170 GeV$< \hat{p}_T <$ 230 GeV, where $\hat{p}_T$ is the transverse momentum of the parton in the process.

To check whether the calibration reduced the variation with respect to η and E_T as desired, Figure 4.3 shows the detection efficiency as a function of the generated jet E_T for a certain E_T-cutoff, using the calibrated E_T instead of the measured L1 E_T. Three things are worth noticing. Firstly, the differences in the behaviour of the efficiency for the different η-intervals are small, though not zero. Secondly, the 50 % detection efficiency corresponds to an E_T value that more-or-less corresponds to the cutoff value of 40 GeV. Thirdly, the transition from a low to a high efficiency is happening in a short E_T interval, effectively leading to a sharp selection on the real jet E_T.

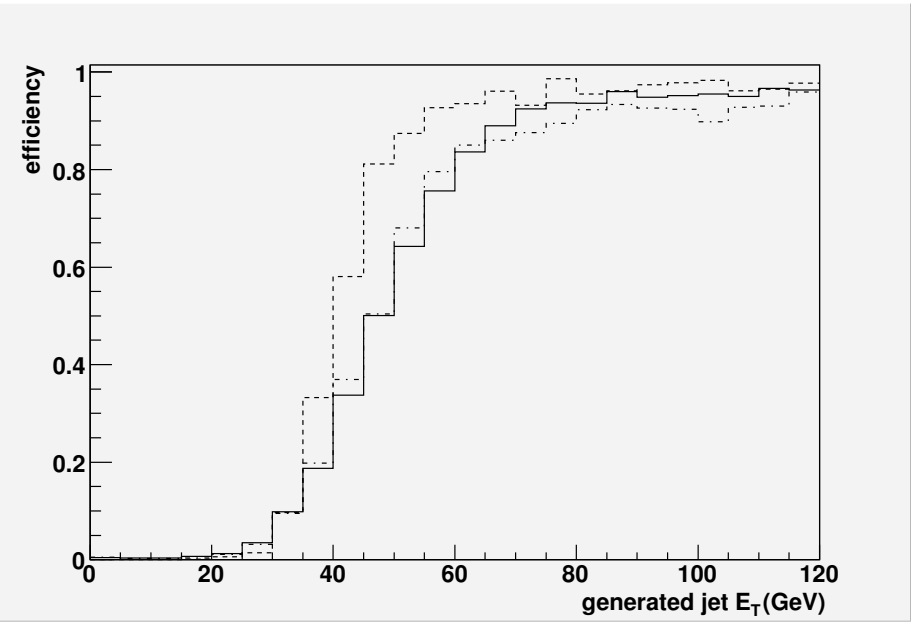

Figure 4.3: Detection efficiency for jets with calibrated $E_T > 40$ GeV as a function of generated jet E_T. The full line shows jets with $|\eta| < 1.5$, the dashed line jets with 3.0 $< |\eta| <$ 5.1 and the dotted line jets with 1.5 $< |\eta| <$ 3.0.

4.2 Invariant masses of jet combinations

The invariant mass of two jets is given by

$$m_{inv}^2 = (E_1 + E_2)^2 - |(\vec{p_1} + \vec{p_2})|^2 \tag{4.1}$$

$$m_{inv}^2 \approx 2 * E_1 * E_2 * (1 - \cos\theta_1 * \cos\theta_2 - \\ - \sin\theta_1 * \sin\theta_2 * \cos(\phi_1 - \phi_2)) \tag{4.2}$$

where the following relations have been used

$$\vec{p} \approx E * \sin\theta * \cos\phi * \vec{\hat{x}} + E * \sin\theta * \sin\phi * \vec{\hat{y}} + \\ + E * \cos\theta * \vec{\hat{z}} \tag{4.3}$$

$$m_{1or2} << E_{1or2} \tag{4.4}$$

$$E = E_T * \cosh\eta \tag{4.5}$$

$$\theta = 2 * \arctan e^{-\eta} \tag{4.6}$$

The invariant masses reconstructed from the jets, for a Higgs with a mass of 120 GeV, is shown in Figures 4.5 - 4.7.

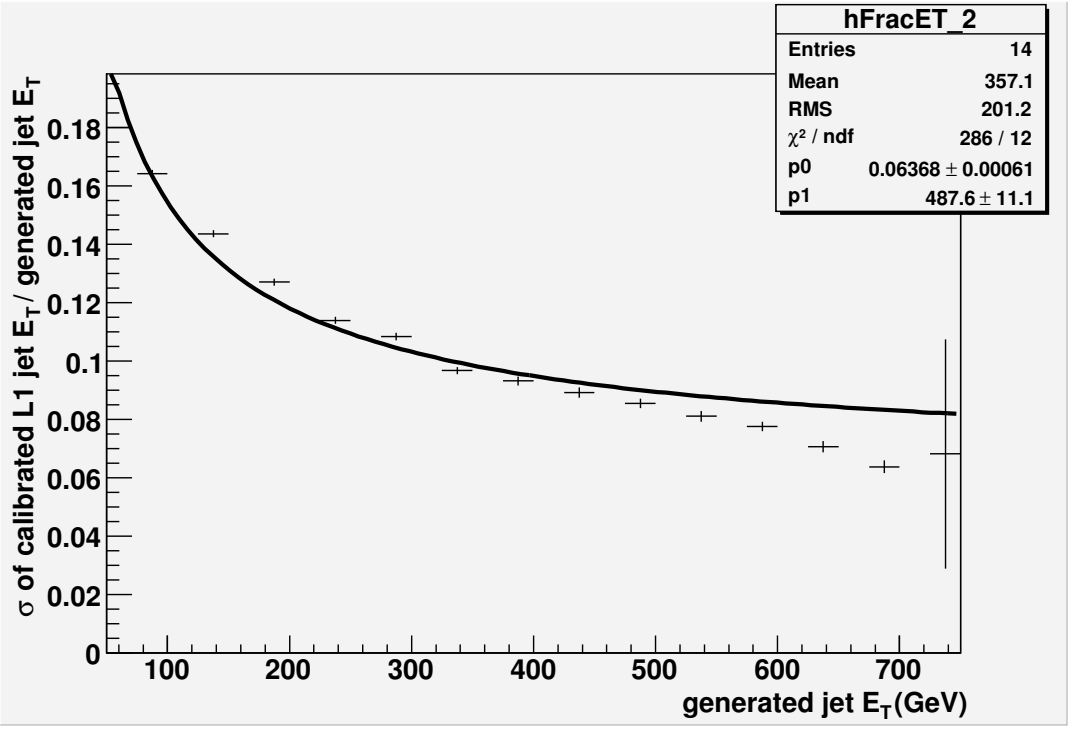

Figure 4.4: Gaussian width of the distribution of the ratio of the calibrated jet E_T and the generated E_T as a function of the generated E_T for central L1 jets ($|\eta| < 3.0$). Superimposed is the best fit giving a resolution $\sigma(E_T)/E_T = p0 \oplus p0 * \sqrt{p1} = (6.37 \pm 0.06)\% \oplus (141 \pm 2)\%/\sqrt{E_T[\text{GeV}]}$. See the text on page 56 for more details.

Figure 4.5 shows the invariant mass distribution for the largest two generated jets, which shows the expected maximum mass corresponding to the Higgs mass, with an extended tail to shorter masses, since the two bottom-quarks from the Higgs decay will not always decay to just two observable jets, because of the significant probability that one of them emits a hard gluon giving a third final state jet.

Figure 4.6 shows the invariant mass distribution for the two L1 jets in events with exactly two jets detected at L1. Here the peak has shifted to much lower masses, and the detector effects have smeared the distribution, so it is more symmetric around its maximum.

Finally, Figure 4.7 shows the invariant mass distribution for the two largest calibrated L1 jets having an E_T above 40 GeV in events with at least two L1 jets detected at L1, using the jet E_T correction described in Appendix A. This distribution shows a larger resemblance to the distribution for the generated jets and is centered at the cor-

rect Higgs mass. The small peak near zero can be removed by also demanding that the difference between the angles of the jets in the transverse plane to the beam be near π, which one would expect also to reduce the QCD background at low invariant masses.

A corresponding invariant mass rate distribution for the background is shown in Figure 4.8, and resembles the distribution of the Higgs sample, except for the long tail to larger E_T's. Thus it is not a surprise that a back-to-back condition for the jets ($|\Delta\phi - \pi| < 0.4$) shown in Figure 4.9 only reduces the background by $\sim 10\%$. However, an invariant mass cut does look useful, since it can be seen in Figure 4.9 to have an efficiency of around 15% for signal generated with ExHuME (identical for EDDE, not shown) while it reduces the background by a factor 150. The conclusion is that the invariant mass of the two largest jets can be used for selecting Higgs events, but only if the Higgs mass is already well known.

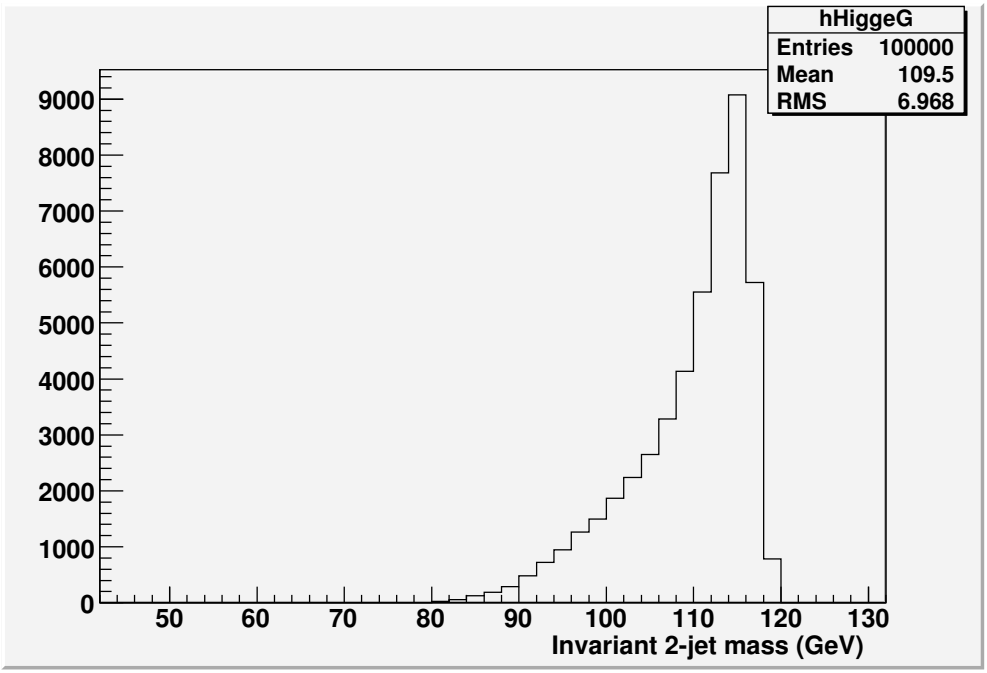

Figure 4.5: Invariant mass of largest two generated jets, when demanding generated $E_T > 40\ GeV$ for a Higgs with a mass of 120 GeV without taking detector effects into account.

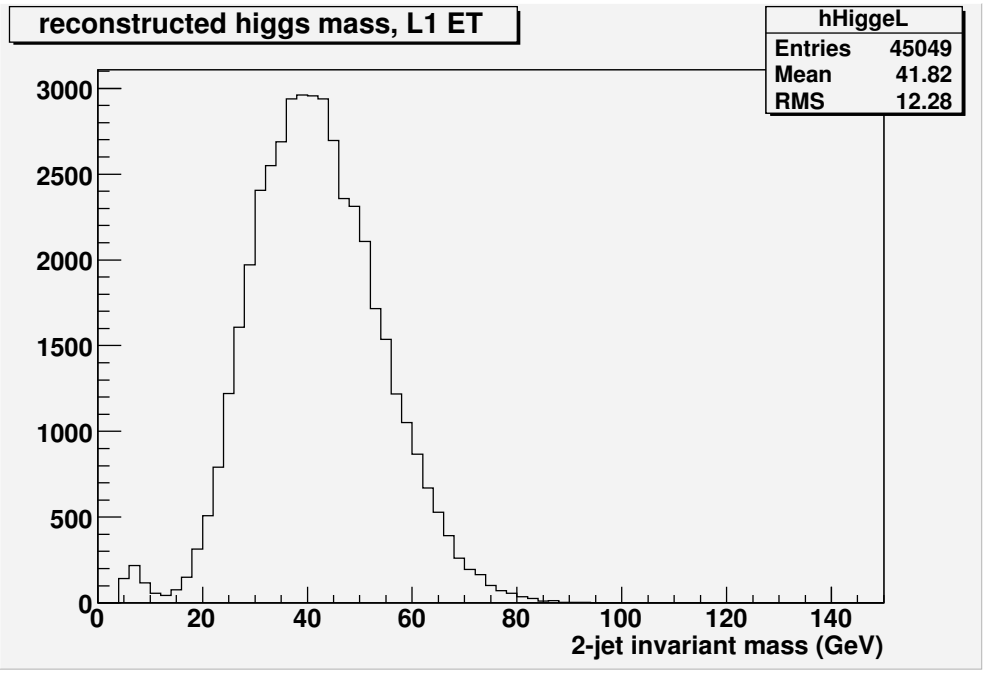

Figure 4.6: Invariant mass of two L1 jets reconstructed from the measured L1 jet E_T for events with exactly two L1 jets for a Higgs with a mass of 120 GeV, including detector effects.

4.3 Muon triggers present and future

Since a light Higgs boson decays to $b - \overline{b}$-quark pair, or if it is a little more massive also to W^+W^-, both of which have muon-rich decay products, some interesting L1 triggers are the already implemented 1μ and 2μ triggers. In addition, some trigger with muons and jets is interesting, since the Higgs decay will contain both, and the pure L1 2-jet trigger cannot be extended to low enough E_T without exceeding the allowed sub-trigger rate of O(1 kHz) already at a luminosity of $10^{32}\ cm^{-2}s^{-1}$. Figure 4.10 shows the trigger rate as a function of the L1 muon transverse momentum[2] (P_t) threshold and Figure 4.11 the signal efficiency as a function of the L1 muon threshold. At a luminosity of $2 * 10^{33}\ cm^{-2}s^{-1}$ the 1μ trigger p_T threshold is expected to be approximately 14 GeV, leading to an efficiency of 6 % for a 120 GeV Higgs. A $1\mu + 1jet$ trigger could have a lower muon p_T threshold around 4-6 GeV, giving an additional 3-5 % of efficiency. These thresholds are a little lower than the latest version of the corresponding

[2]the component of the muon momentum perpendicular to the magnetic field used for bending the trajectory of the muon.

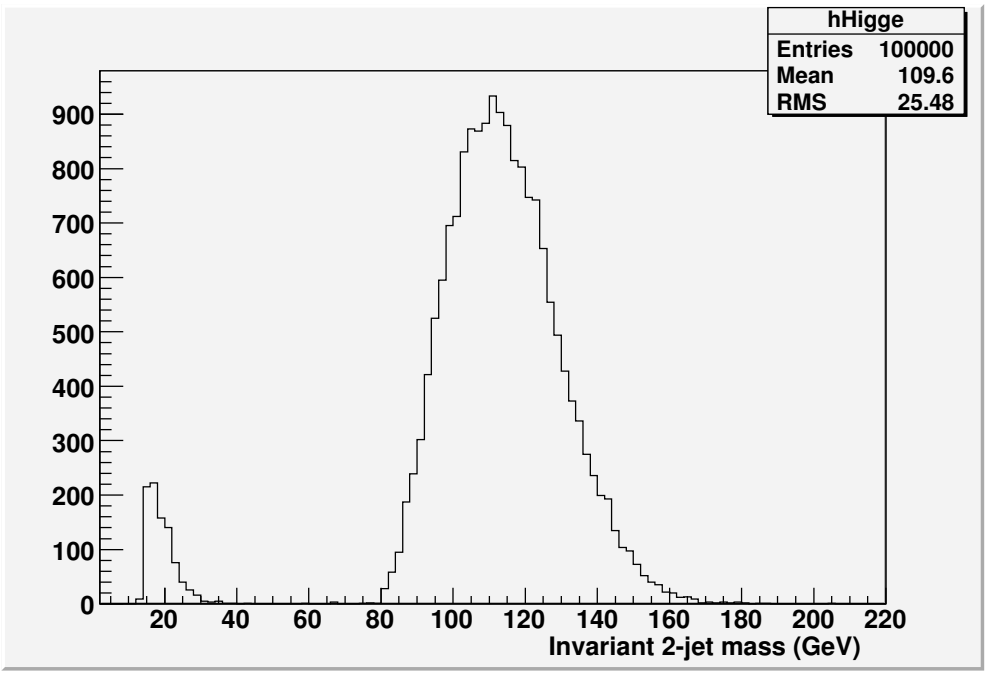

Figure 4.7: Invariant mass of the two L1 jets with the largest E_T for events with at least two L1 jets with a corrected E_T above 40 GeV, for a Higgs with a mass of 120 GeV, including detector effects and jet E_T calibration.

High Level Trigger (HLT) thresholds [36] of 19 GeV and 7 GeV, but at HLT there is more information available from the Roman Pots, among other things, which should compensate for this shortfall.

The 2-muon trigger rate is shown in Figure 4.12 giving an assumed second muon p_T threshold of 2-4 GeV. A 2-muon trigger efficiency of around 2 % can be extracted from Figure 4.13 using such a threshold. However, if the $1\mu + 1jet$ trigger is implemented, it will presumably overlap somewhat with the 2μ trigger so that a fraction of the events triggering the 2μ trigger also trigger the $1\mu + 1jet$ trigger.

The muon triggers and other triggers based only on the central ($|\eta| < 5$) muons and jets are complementary to the Roman Pot triggers studied by Richard Croft (see Ref. [37]) since an L1 trigger demanding hits in the Roman Pots only, has an efficiency of around 20 % and a low enough background rate only up to luminosities a few times $10^{32} cm^{-2} s^{-1}$. On the other hand, by adding central L1 objects to the trigger, one may reduce the background appreciably, and so reach higher luminosities. Naturally the Roman Pots are also useful in lowering the background rate of L1 triggers based only on central objects; for example an L1 trigger demanding two jets above threshold

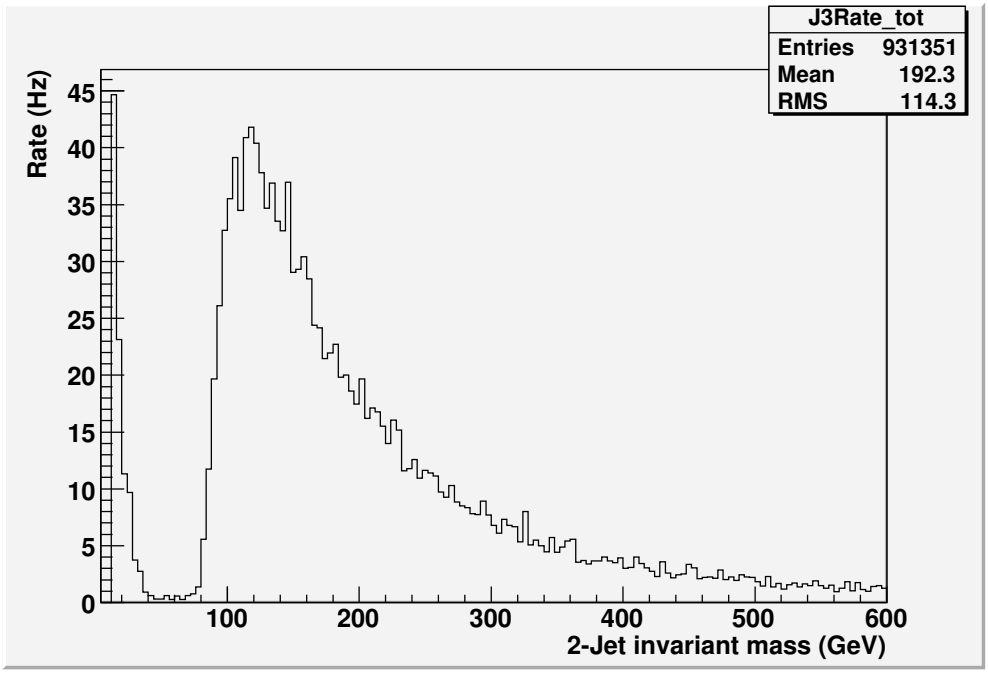

Figure 4.8: Rate of 2-jet invariant mass of calibrated jets for the QCD background sample for a luminosity of $10^{32} cm^{-2} s^{-1}$. Only events with at least two calibrated L1 jets with an E_T above 40 GeV were considered.

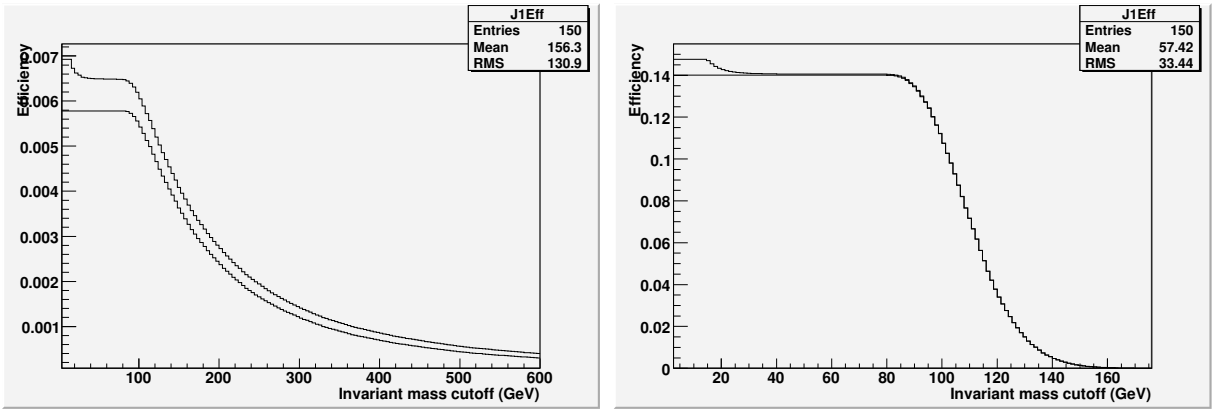

Figure 4.9: Fraction of events with 2-jet invariant masses above a cutoff value. On the left is the QCD background sample, and on the right the ExHuME Higgs sample. The Higgs sample from EDDE gives an almost identical figure as the one from ExHuME. For the lower curves the jets are in addition demanded to be back-to-back in azimuthal coordinates ($|\Delta\phi - \pi| < 0.4$)

has too high a threshold to be useful in finding the Higgs above a luminosity of a few times $10^{32} cm^{-2} s^{-1}$ too, because of pileup. Also, by using central objects-only triggers one can gain around ten percent of signal efficiency from the muon triggers alone that should overlap little with the events reaching the Roman Pot. Furthermore, by triggering on an appreciable fraction of the events having both protons detected in the proposed Roman Pots at 420 m [15] from the interaction point, many events are saved for the higher trigger levels where the missing invariant mass of the central system can be easily reconstructed from the two forward protons. These Roman Pots cannot be used to trigger at L1 on their own since they are so far away from the IP that the trigger signal from them arrives after the time the L1 decision for that event has to be taken.

4.4 A somewhat more massive Higgs

The Higgs boson dominantly decays to a particle-antiparticle pair of the most massive particle with a mass less than half the Higgs mass, since the Higgs couples to the mass of elementary particles. This implies that a very light Higgs decays dominantly to $b-\overline{b}$ for Higgs masses up to around 140 GeV. Above 140 GeV W^+W^- starts to dominate, since $2 * M_W \approx 161$ GeV, and the off-mass-shell W suppression factor is less than the ratio between the couplings to W^+W^- and $b - \overline{b}$ for the Higgs.

The W^+W^- decay mode gives on the average rise to more primary decay jets than the two in the previously considered case of a Higgs with a mass of 120 GeV, thus lowering the average E_T of any of them, making them more difficult to reconstruct. In fact, if four L1 jets are required, only 0.6% of the signal events are accepted, compared to the 47% expected from the branching fraction.

Because the W-boson branching ratio to $\mu + \nu_\mu$ and $\tau + \nu_\tau$ are each 11% [5], and 17% of the τ leptons subsequently decay to muons, W^+W^- Higgs events are more muon rich than $b-\overline{b}$ Higgs events. Therefore, the one muon trigger has an efficiency of 16 %, with a 14 GeV p_T threshold (See Figure 4.14). Because of the lower average jet E_T, the $1\mu + 1jet$ trigger brings only an additional 1.5 % efficiency. A 2-muon trigger efficiency of around 1.5 % was found for a 140 GeV Higgs decaying to W^+W^- for an assumed second muon p_T threshold of 2-4 GeV.

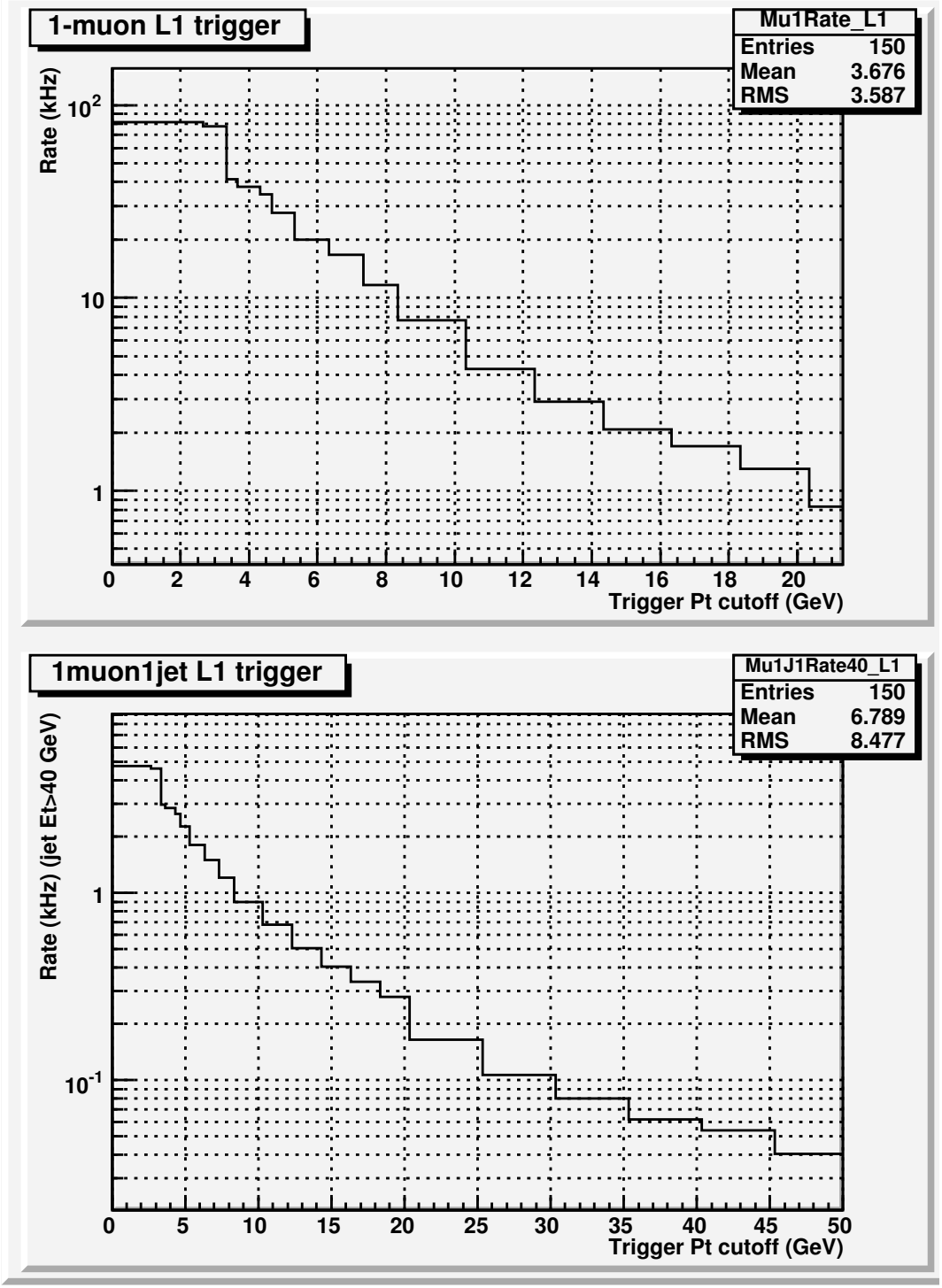

Figure 4.10: Expected trigger rate for a 1μ (upper plot) and $1\mu + 1jet$ (lower plot) trigger for QCD background, at a luminosity of $2 * 10^{33}\ cm^{-2}s^{-1}$. The jet energy threshold is 40 GeV.

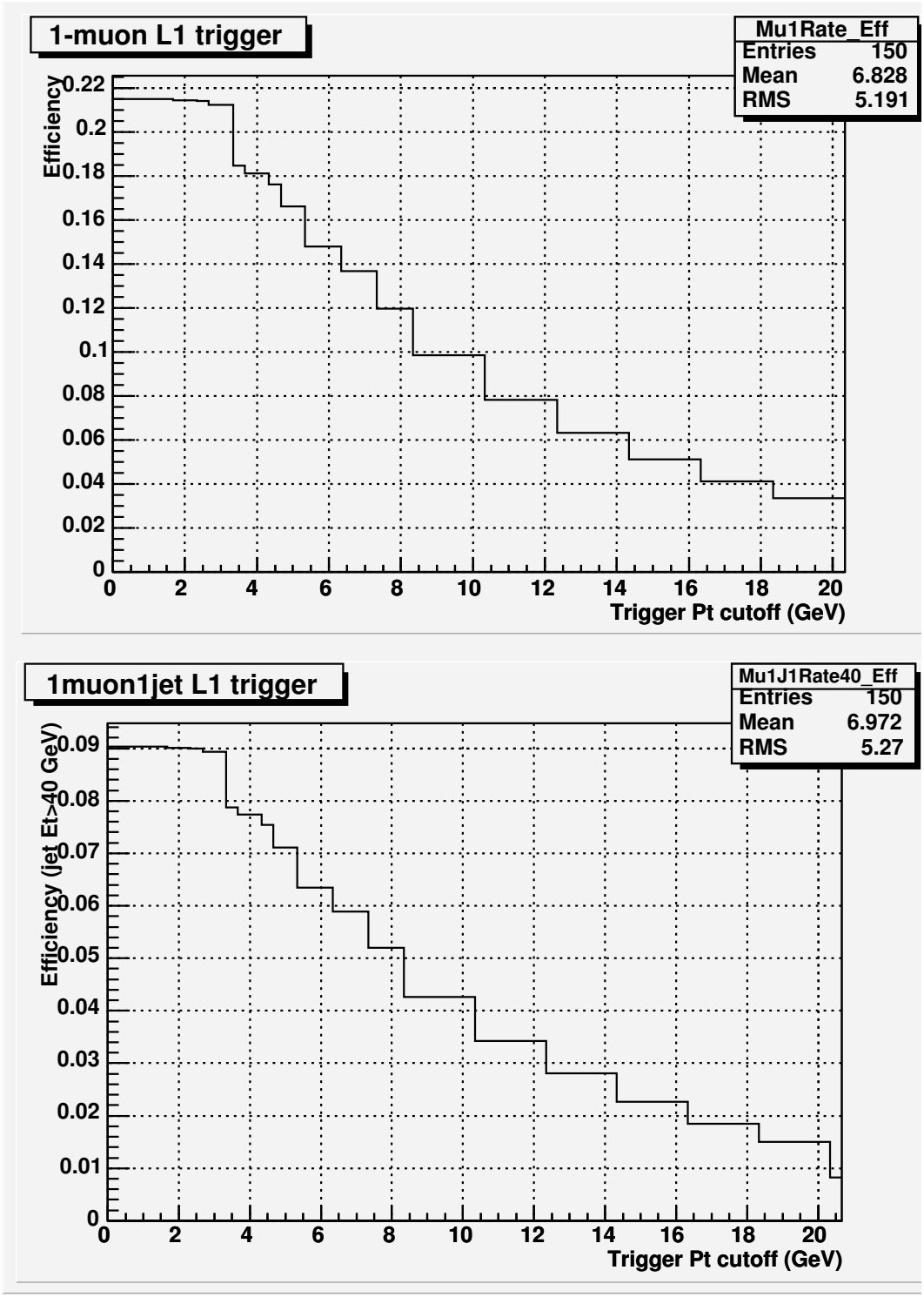

Figure 4.11: Signal efficiency for the 1μ (upper plot) and $1\mu + 1jet$ (lower plot) trigger for diffractive Higgs events for a Higgs with a mass of 120 GeV. The jet energy threshold is 40 GeV. The Higgs sample was generated with ExHuME.

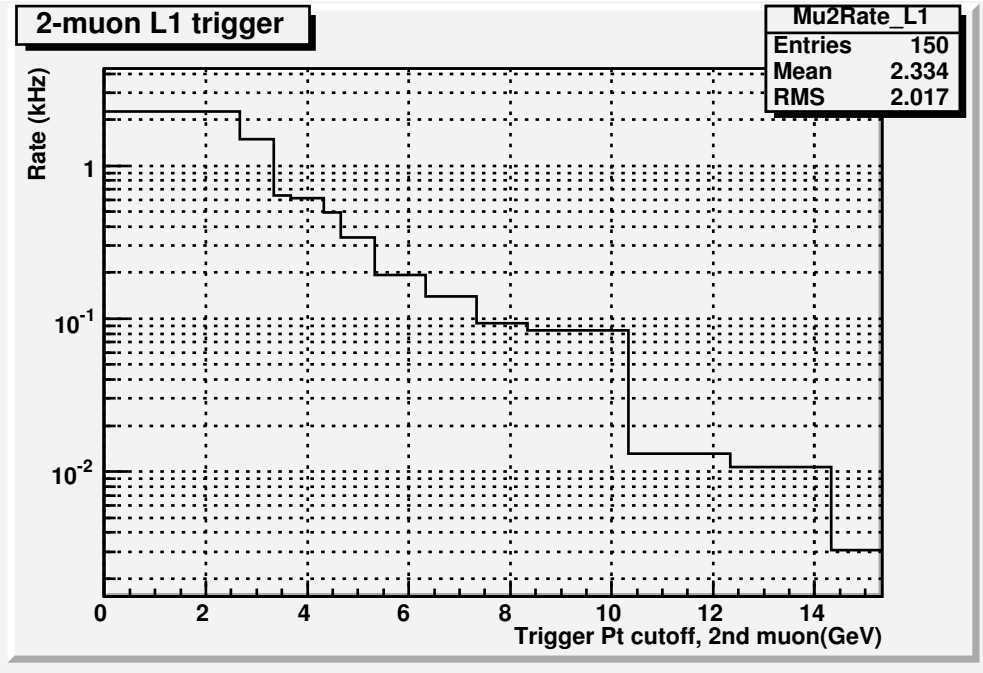

Figure 4.12: Expected trigger rate from QCD background for the 2μ trigger, at a luminosity of $2 * 10^{33}\ cm^{-2}s^{-1}$.

Figure 4.13: Signal efficiency for the 2μ trigger for diffractive Higgs events for a Higgs with a mass of 120 GeV. The Higgs sample was generated with ExHuME.

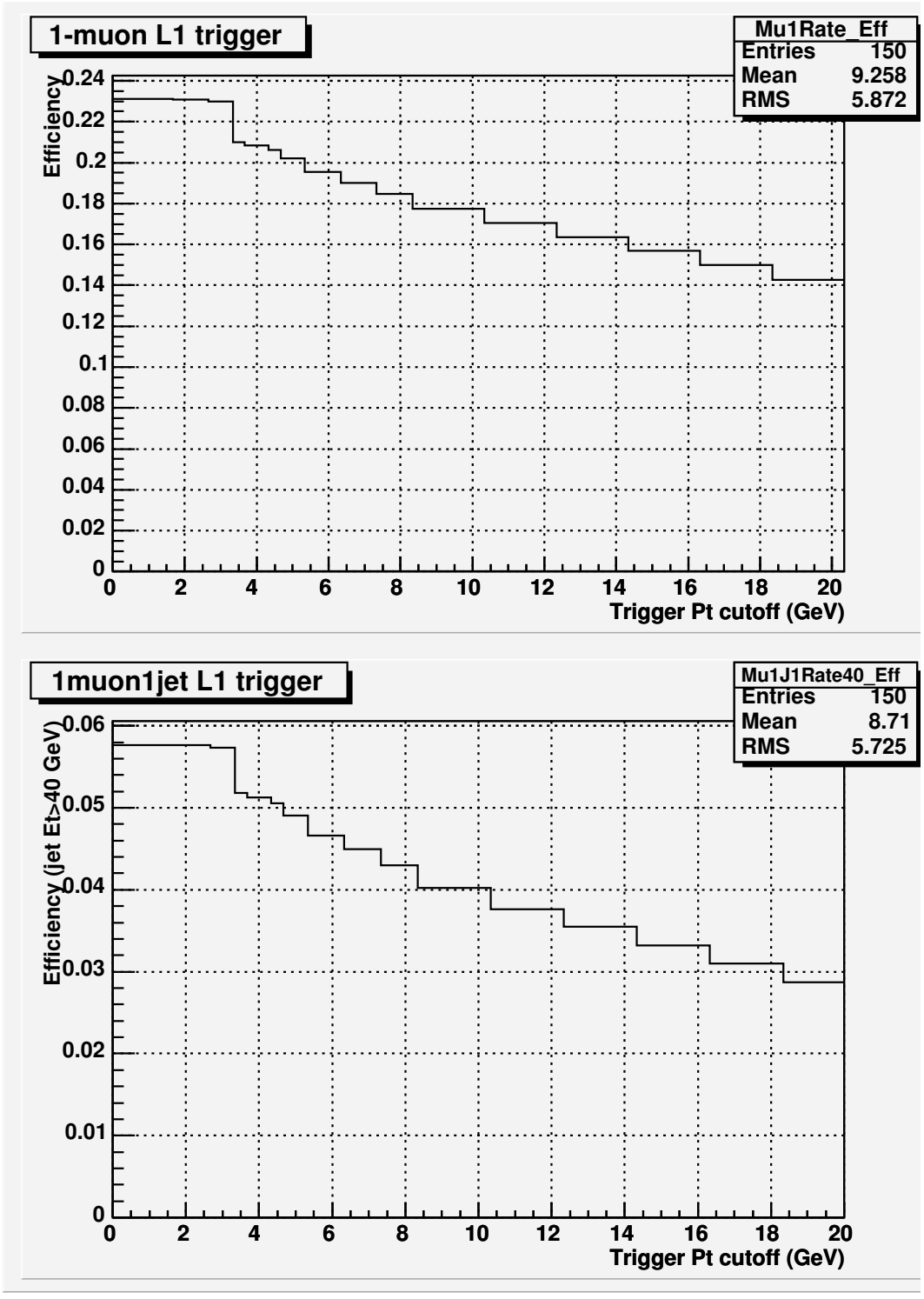

Figure 4.14: Signal efficiency for the 1μ and $1\mu + 1jet$ trigger in diffractive Higgs events for a Higgs with a mass of 140 GeV decaying to a W^+W^- pair. The jet energy threshold is 40 GeV. The Higgs sample is generated with ExHuME.

4.5 Scalar sum of L1 jet E_T

Since a light Higgs decays mostly to two jets, an interesting variable to look at is the sum of the $E_T's$ of the two largest jets in an event divided by the sum of all jets in that event, since the sum of the E_T of all identified jets is available at L1 as a parameter called H_T. Figure 4.15 shows the efficiency of such a requirement for a Higgs sample generated with EDDE and its background acceptance. The trigger uses the parameter $(E_T^{Largest}+E_T^{2ndLargest})/\sum_i E_T^i$ evaluated for each event, except if either of the two jets are below $E_T = 40GeV$. Figure 4.16 shows the same thing, only now the two jets are in addition required to be central ($|\eta| < 3$). The improvement in the signal to background ratio is the ratio of the signal efficiency and the background acceptance, as shown in Figure 4.17. A condition like $(E_T^1 + E_T^2)/H_T > 0.9$, which was proposed in Ref. [37] can be evaluated. From Figures 4.15-4.18 it can be seen that such a condition might be useful as an additional one for background-dominated triggers like two central jets above $\sim$ 40 GeV; in this case the signal to background ratio was increased by $\sim 40\%$, while $\sim 12\%$ of the signal was retained. However, the H_T condition by itself has about the maximum allowable background rate already at a luminosity of $10^{32} \quad cm^{-2}s^{-1}$, as can be seen in Figure 4.18.

4.6 Back-to-back criterion for the two largest L1 jets

Since a light Higgs decays mostly to two jets, another variable to investigate is the difference in the ϕ-coordinate between the two largest E_T jets. This variable is interesting because if there are only two decay jets, they should be exactly antiparallel in the Higgs rest frame. Now, the η coordinates of the jets in the lab frame will in general not be of equal magnitude and opposite sign like in the rest frame, due to a boost of the produced Higgs in the beam direction. However, the back-to-back condition will be maintained in the transverse plane, so the difference between the two azimuthal angles of the two jets should still be around $|\phi_1 - \phi_2| \approx \pi$. Due to the coarse ϕ-reconstruction at L1, the ϕ angles will only be back-to-back with a precision corresponding to the L1 granularity of $\sim 0.3\, rad \approx 20°$. The efficiency of a 2-jet trigger plus a back-to-back condition was investigated. The latter was chosen to be $|\Delta\phi| > 2.7$, where $\Delta\phi$ is defined to be the smaller angle between the jets in the transverse plane, i.e. $0 \leq |\Delta\phi| < \pi$. By taking the ratio of the trigger with the ϕ cut and the one without, one obtains the fraction of the events having 2 jets above a threshold,

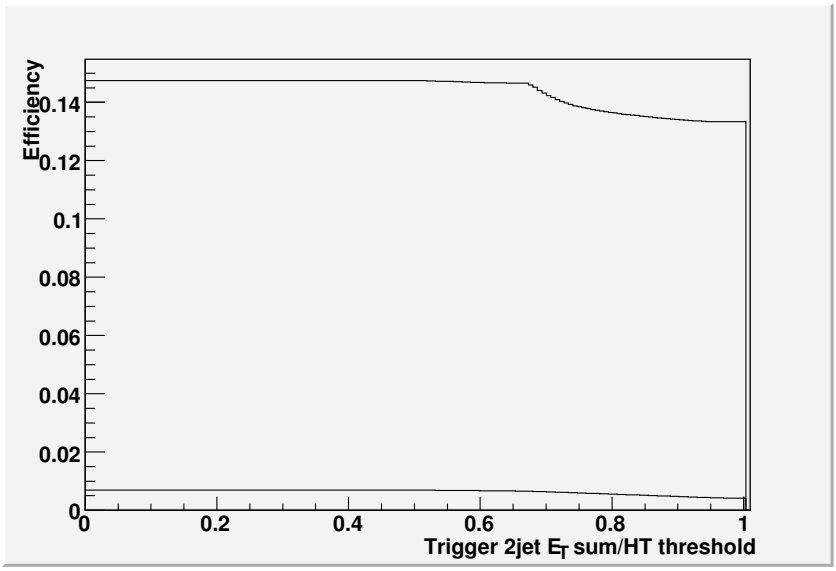

Figure 4.15: Efficiency for a 2-jet E_T sum/H_T requirement at L1. H_T is the sum of the $E_T's$ of all L1 jets, not just the 12 jets available as L1 trigger objects. The calibrated jet E_T is used. The upper curve is for the EDDE Higgs sample and the lower for the QCD background.

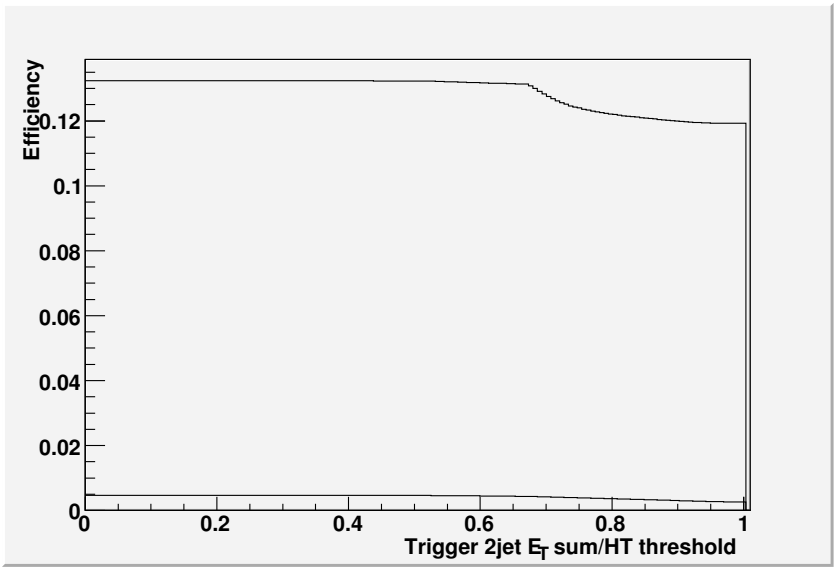

Figure 4.16: Efficiency for a 2-jet E_T sum/H_T requirement at L1. The jets are required to be central, i.e. within $|\eta| < 3.0$. H_T is the sum of the $E_T's$ of all L1 jets, not just the 12 jets available as L1 trigger objects. The calibrated jet E_T is used. The upper curve is for the EDDE Higgs sample and the lower for the QCD background.

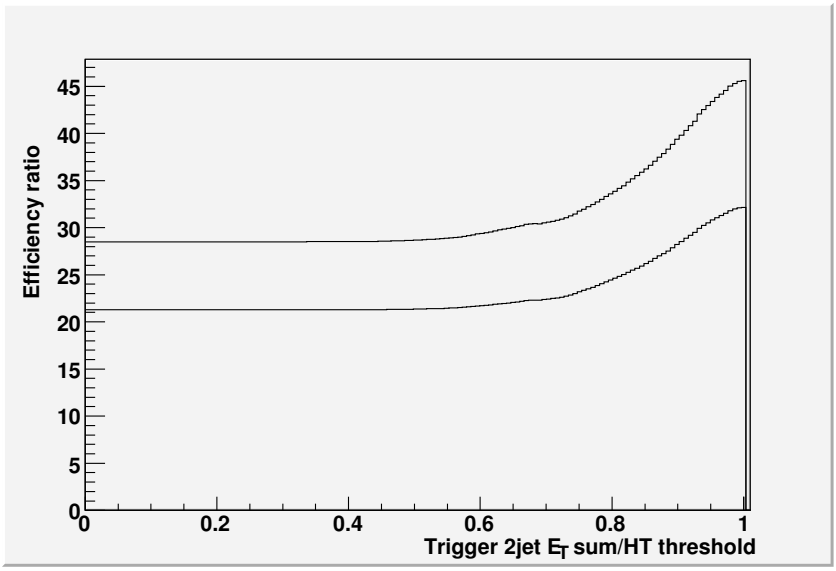

Figure 4.17: Efficiency ratio as a function of a 2-jet E_T sum/H_T threshold requirement. H_T is the sum of the $E_T's$ of all L1 jets. The calibrated jet E_T is used. The upper curve is for central jets and the lower for all jets.

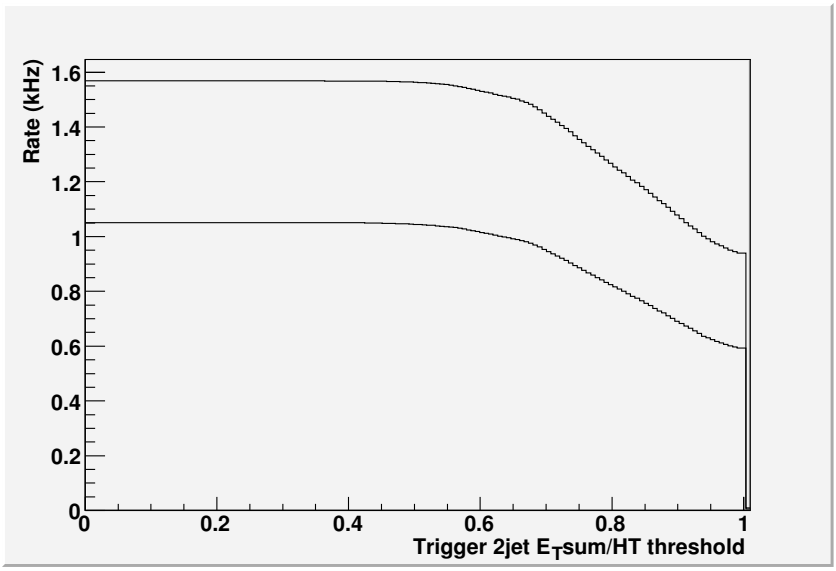

Figure 4.18: Background rate at a luminosity of $10^{32}\ cm^{-2}s^{-1}$ for a trigger requiring at least two jets above an E_T of 40 GeV as a function of a 2-jet E_T sum/H_T threshold requirement. H_T is the sum of the $E_T's$ of all L1 jets. The calibrated jet E_T is used. The lower curve is for central jets ($|\eta| < 3$) and the upper for all jets. The rate at a threshold of 0 is equal to the 2-jet rate with no H_T condition.

for which these jets are back to back. In Figure 4.19 the 2-jet efficiency is shown, in Figure 4.20 the 2-jet plus ϕ cut, and in Figure 4.21 the ratio of the two efficiencies for the Higgs signal and the background. Since the jet E_T threshold cannot be lower than around 40 GeV, and because the majority of Higgs jets have an E_T at or below $\sim$ 60 GeV such a trigger would have a background acceptance of above 80% and a signal efficiency around 90%, as shown in Figure 4.21, making it unusable.

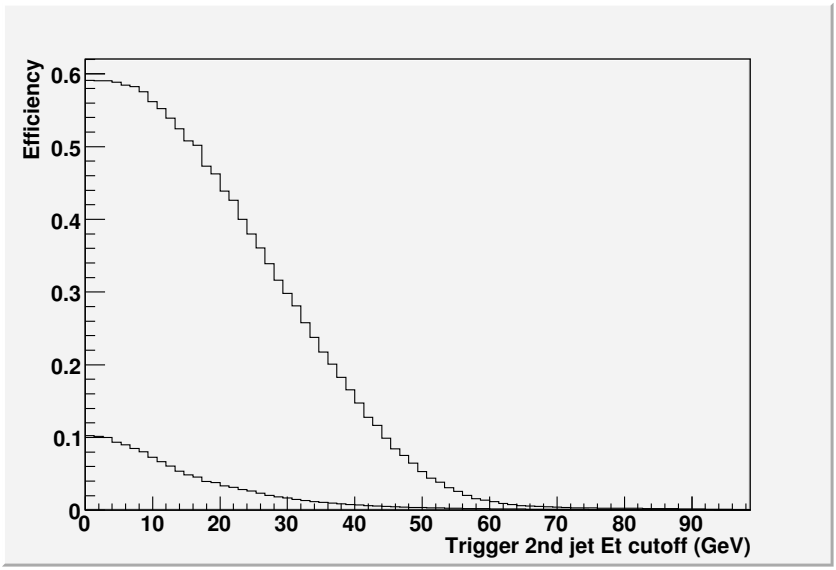

Figure 4.19: Trigger efficiency for 2 jets above an E_T threshold. The calibrated jet E_T is used. The upper curve is for EDDE Higgs events and the lower for QCD background events.

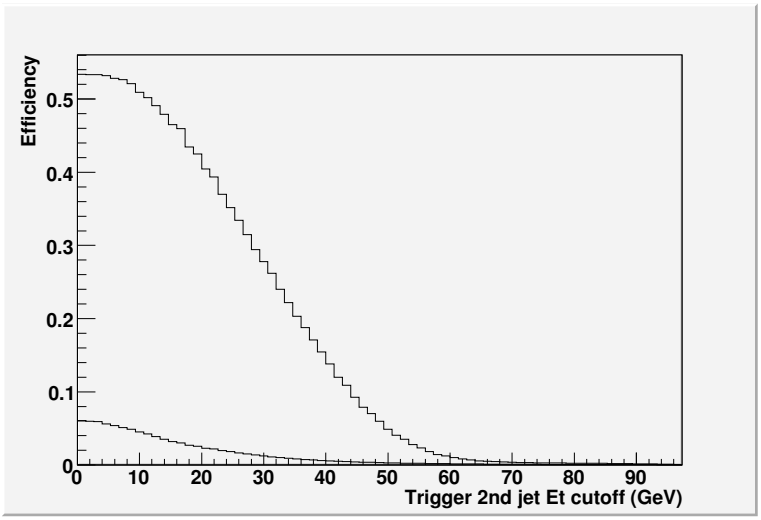

Figure 4.20: Trigger efficiency for 2 back-to-back jets above an E_T threshold. The back to back requirement is $|\phi_{jet1} - \phi_{jet2}| > 2.7, 0 \leq |\Delta\phi| < \pi$. The calibrated jet E_T is used. The upper curve is for EDDE Higgs events and the lower for QCD background events.

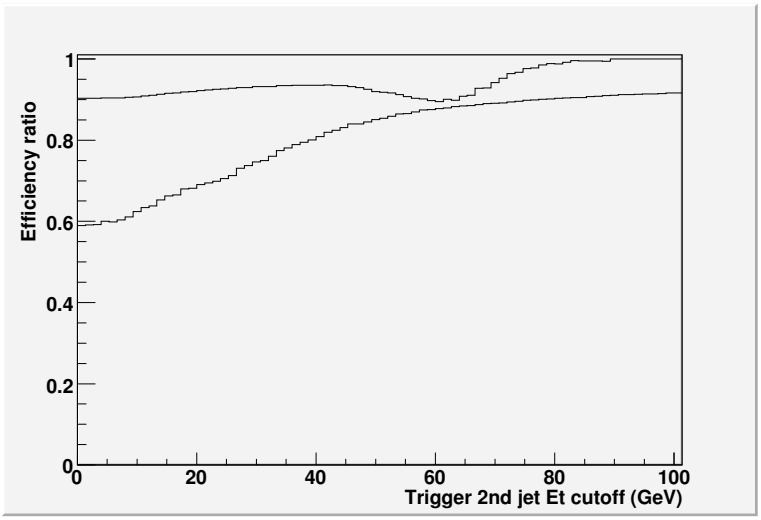

Figure 4.21: Partial efficiency for a back-to-back condition on the two largest E_T jets above a threshold, i.e. the ratio of the efficiencies for a 2-jet trigger and a trigger requiring the two jets plus $|\phi_{jet1} - \phi_{jet2}| > 2.7, 0 \leq |\phi_1 - \phi_2| < \pi$ as a function of the E_T threshold. The calibrated jet E_T is used. The upper curve is for EDDE Higgs events and the lower for QCD background events.

Chapter 5

Conclusions

In this thesis I investigated proposed and accepted CMS/TOTEM L1 triggers composed of various combinations of L1 objects, and their signal efficiency and background rate in finding a diffractively produced low-mass Higgs.

I found that the muon triggers combined give an efficiency of about 8% if the Higgs decays predominantly to $b\bar{b}$ and about 17 % if the Higgs decays dominantly to W^+W^-. By adding an L1 trigger combining a muon and a jet, the $H \rightarrow b\bar{b}$ trigger efficiency can be increased to $\sim 12\%$. Such a trigger would not significantly increase the efficiency in the $H \rightarrow W^+W^-$ channel. These triggers will complement the trigger using 2 jets in the central CMS detectors plus a proton in the closeby Roman Pots at 220 m from the IP, as proposed in Ref. [37].

The invariant mass of the 2 jets could also be used to reduce the background rate with the caveat of introducing mass dependencies in the triggering. This is probably not desirable, at least not before one knows the Higgs mass more precisely than the present indirect measurement of 114 GeV$< M_H <$300 GeV, at 95% confidence. A trigger based on the sum of the two largest jet E_T's as a fraction of total E_T, turned out to improve the signal to background ratio by around 40%. It could thus be used as an extra condition in background-dominated triggers like the simple 2-jet L1 trigger. In contrast, a trigger based on the difference in the ϕ coordinate between the two jets turned out to be useless at the foreseen jet E_T threshold.

I also studied the measured E_T of L1 jets, which on the average corresponds to only around 60 % of the real jet E_T, varying also as a function of the rapidity of the jet. To remedy the situation using only information available at L1, I looked for an algebraically simple calibration function, which I chose to be two parabolas joined to-

gether, within the region where they are monotonically growing. Using the calibration, the E_T resolution was improved to $\sigma(E_T)/E_T = 6.4\% \oplus 140\%/\sqrt{E_T[\text{GeV}]}$ for L1 central ($|\eta| < 3.0$) jets .

To summarize: a diffractively produced Standard Model low mass Higgs should be triggered with a substantial efficiency at the first trigger level at the LHC, provided that the theoretical predictions of cross section of a few femtobarns are correct.

Further detailed high trigger level and offline studies are necessary to validate the feasibility of detecting a diffractively produced Standard Model low mass Higgs after the LHC has collected $O(30\,\text{fb}^{-1})$, i.e. when the sample of events for this signal-dominated process should be large enough to claim a 5-7 standard deviation Higgs signal.

Appendix A

Transverse energy correction for L1 jets in CMS[1]

A.1 Abstract

We describe a method for calibrating the transverse energy (E_T) of jets reconstructed by the first level (L1) trigger in CMS. Corrections are made as a function of both pseudorapidity (η) and transverse energy based on simulated PYTHIA QCD events. Special emphasis has been made to extend the validity of the calibration to as low E_T jets as feasible. The transverse energy resolution for L1 central ($|\eta| < 3.0$) jets after the calibration is found to be $\sigma(E_T)/E_T = 6.4\% \oplus 140\%/\sqrt{E_T[\text{GeV}]}$.

A.2 Introduction

The ability to reliably trigger on level one (L1) jets is crucial both for many Standard Model measurements as well as for new physics searches at the LHC. This is especially relevant for the forward physics program of the combined CMS/TOTEM running, where the interesting jets are expected to have a fairly low transverse energy (E_T), examples of such process can be found in Ref. [38] and [25]. A calibration of the measured L1 jet energy is essential, since only approximately 60 % of the jet energy is detected and there are also large variations as function of pseudorapidity (η) and E_T due to the experimental apparatus and its response to particles. This note describes the calibration of the E_T of jets reconstructed by the L1 trigger of CMS. Special atten-

[1] F. Oljemark, K. Österberg and M. Grothe, CMS internal note, CMS IN-2006/040.

tion is put on having a valid calibration also for jets down to E_T's of about 30 GeV. The resulting jet E_T calibration is automatically applied to all reconstructed L1 jets in ORCA from the version 8.13.1 onwards. The previously valid L1 jet E_T calibration can be found in Ref. [39].

At L1, jets are reconstructed using the calorimeter response by dividing the complete calorimetry coverage into $22 * 18$ regions in the (η, ϕ)-plane[2]. This aggregates $4 * 4$ calorimeter towers into one L1 calorimeter region (coarsening the resolution by a factor four in both ϕ and η). Then a $3 * 3$ calorimeter region window is slid across the (η, ϕ)-plane, and a new jet is declared to be the $3 * 3$ calorimeter region window with the largest E_T sum such that the central region in the $3 * 3$ window has a larger E_T than any of its neighbours. The E_T of the jet is set to equal to the E_T sum of the regions in the $3 * 3$ window and its coordinates equal to those of the central region. Since no weighted average is computed, this further degrades the angular localization of the jet. The used regions are then zeroed and the next jet is iteratively searched for using the same algorithm until all jets above a 5 GeV threshold are found. At the global calorimetric L1, the information from at most twelve jets (the four most energetic central, the four most energetic central "τ" and the four most energetic forward jets) is available as well as the E_T sum of all the reconstructed L1 jets. In this study, no distinction has been made between the thinner L1 "τ" jets and standard L1 jets since many QCD and b-jets, especially at low E_T's, are tagged as "τ" jets at L1.

A.3 Event sample used

The QCD jet events used for the calibration were generated with PYTHIA [30] version 6.3. A jet-finding algorithm was run on the final state particles to provide a list of generator-level jets as input to the study. The full simulation of the CMS detector was performed with OSCAR 2.4.5 for the QCD sample and with OSCAR 3.6.5 for an ExHuME [32] version 1.0 test sample consisting of low E_T b-jets. The L1 reconstruction was done with ORCA 7.6.1 for the QCD samples and ORCA 8.7.1 for the ExHuME samples providing the reconstructed L1 jets in the form of a ROOT ntuple that was analyzed. All the used samples were produced on the Wisconsin CMS Tier-2[3]. See table A.1 for values on some of the parameters used for simulating the calorimeters.

[2] $\eta \equiv -\ln(\tan(\theta/2))$ and θ (ϕ) is the polar (azimuthal) angle with respect to the direction of the clockwise turning beam.

[3] www home-page: http://www.hep.wisc.edu/cgi-bin/cms/CMSJug.cgi?p=datasets

Table A.1: The energy thresholds and noise levels used in the study. p.e. = photo electrons.

Parameter	Barrel	Endcap	Very Forward
ECAL digi threshold	90 MeV	450 MeV	-
HCAL digi threshold	500 MeV	500 MeV	500 MeV
Noise level ECAL	40 MeV	150 MeV	-
Noise level HCAL	3 p.e.	3 p.e.	0.125 p.e.

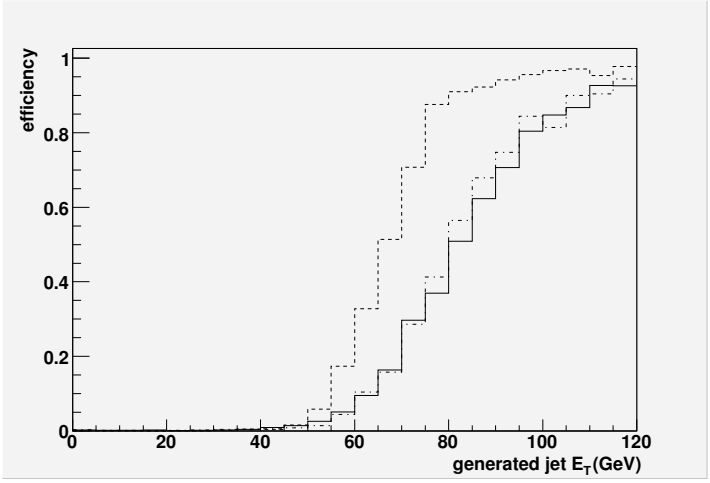

Figure A.1: Detection efficiency for L1 jets with measured $E_T > 40$ GeV as a function of generated jet E_T. The full line shows jets with $|\eta| < 1.5$, the dashed line jets with $3.0 < |\eta| < 5.1$ and the dotted line jets with $1.5 < |\eta| < 3.0$.

A.4 Calibration method

First the reconstructed L1 jets and generator-level jets were correlated with each other by requiring that they were within an angular distance of $\sqrt{\Delta\eta^2 + \Delta\phi^2} < 0.3$ (0.5) in the central (forward) region of the experiment. Then their transverse energies were added as a pair to a two-dimensional E_T(L1) versus E_T(generated) histogram for the η-interval corresponding to the η of the reconstructed L1 jet. The size of an η-interval was approximately 0.35 for the very central region ($|\eta| < 2.2$) and approximately 0.5 for the rest of the calorimeter coverage.

The necessity to make η dependent corrections is illustrated by Figure A.1, where the detection efficiency for L1 jets with measured $E_T > 40$ GeV is shown for three

different ranges in pseudorapidity ($|\eta| < 1.5$, $1.5 < |\eta| < 3.0$ and $3.0 < |\eta| < 5.1$) as a function of the E_T of the corresponding generated jet. From the figure, it can be seen that the η regions show quite different behaviour and also that the 40 GeV E_T-cutoff in reality corresponds to a much higher value (about 65-80 GeV). To have a reliable L1 jet trigger based on a certain E_T-cutoff, the efficiency should show very little η dependence as well as have approximately a 50 % efficiency for jets having a real E_T equal to the cutoff value. The applied corrections must also depend on the measured L1 E_T since it shows a non-linear behaviour with respect to the generated E_T, especially for energies below 50 GeV. This behaviour can be seen in Figure A.2 showing the measured L1 E_T and the generated E_T relation for one η-interval in the forward region and one in the central.

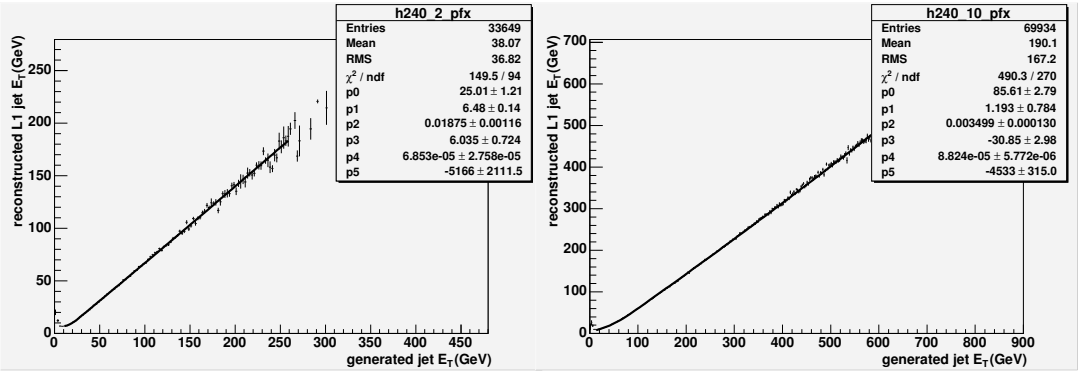

Figure A.2: The measured L1 jet E_T versus the generated jet E_T for the third (left) and eleventh (right) η-interval (-3.839 $< \eta <$ -3.330 and -0.348 $< \eta <$ 0.0, respectively). Superimposed are the double-parabolic calibration fits described in the text. The fitted function as well as the fitted parameters are explained in the Appendix.

A one-dimensional profile histogram as function of the generated jet E_T were made for each η-interval. Each of these profile histograms was then fitted with two separate second-degree polynomials, one for the lower E_T region and one for the higher E_T region, with the additional constraint that the curves had to meet at a common E_T point. This E_T value defined the upper limit of the validity of the low E_T calibration and the lower limit of the validity of the high E_T calibration. The fitted functions were in addition constrained to have their minima to the left of their respective domains of validity so as to be invertible as well as being monotonously growing within the fitted region to ensure a sensible physical behaviour. Two examples of the fits are given in Figure A.2. The above fitting procedure was chosen after trying to fit the whole E_T-

range by means of other types of invertible polynomials without satisfactory results.

The upper edge of the high E_T region fit of each η-interval was chosen such that the statistics for each bin in the fit was sufficient, and the lower edge of the low E_T region fit of each η-interval was set as low a sensible physical behaviour could be ensured. At very low E_T's, the E_T relation between the L1 and generated jet becomes unphysical since a majority of the generated jets are not reconstructed at L1 anymore and those reconstructed tend to have a larger measured E_T than expected. In addition, some other L1 jet caused by remnants of a nearby (necessarily larger) generated jet or simply detector noise could be identified with the generated jet. After ensuring that the E_T ranges used for the fits were good and that all fits had converged correctly, all of the 22 double-parabolic fits were inverted to give the true E_T corresponding to a given measured L1 E_T in a given L1 η-interval.

A.5 Results

As a first cross check, the calibration was applied on a high E_T QCD sample that was not used as input to the calibration. The relative deviation of the calibrated E_T for this sample is shown in Figure A.3 and as expected the mean of a Gaussian fit to the histogram show little deviation from zero. Another check was to remake Fig-

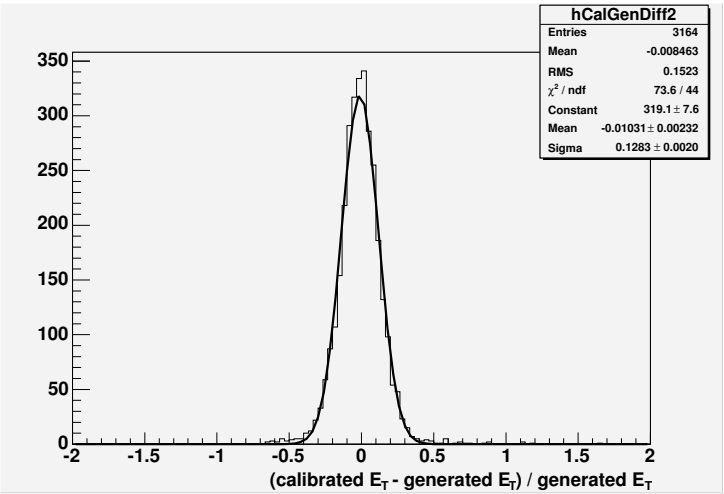

Figure A.3: Fractional deviation of the calibrated E_T from the generated E_T for an independent QCD sample (170 GeV $< \hat{p}_T <$ 230 GeV). The measured L1 E_T was required to be within the domain of validity of the calibration.

ure A.1. Figure A.4 shows the detection efficiency as a function of the generated jet E_T for a certain E_T-cutoff, but using here the calibrated E_T instead of the measured L1 E_T. Three differences between Figures A.1 and A.4 are worth noticing. Firstly, the differences in the behaviour of the efficiency for the different η-intervals are smaller in Figure A.4 than in Figure A.1, though not zero. Secondly, the 50 % detection efficiency now corresponds to a E_T value that more-or-less corresponds to the cutoff value of 40 GeV. Thirdly, the transition from a low to a high efficiency is now happening in a shorter E_T interval, effectively leading to a sharper selection on the real jet E_T.

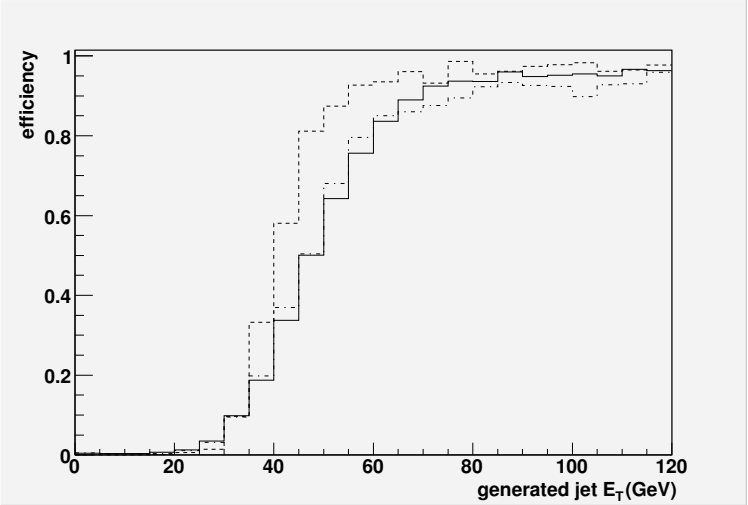

Figure A.4: Detection efficiency for jets with calibrated $E_T > 40$ GeV as a function of generated jet E_T. The full line shows jets with $|\eta| < 1.5$, the dashed line jets with $3.0 < |\eta| < 5.1$ and the dotted line jets with $1.5 < |\eta| < 3.0$.

The calibrated E_T still shows a residual systematic effect for very high and very low E_T's both in the central and forward regions as seen in Figure A.5. The residual systematic effect in the very high E_T region mostly comes from lack of sufficient statistics in the calibration at such E_T's and of course needs to be taken care of offline but is harmless at L1. A residual systematic effect in the low E_T region can potentially be very harmful for the L1 selection and therefore, this low E_T systematic effect was studied in detail. Figure A.6 (left) shows the fractional deviation of the calibrated E_T from the generated E_T as function of the measured L1 E_T for this low E_T region. At most a 5 % relative deviation is visible down to about 15 GeV in measured L1 E_T, which corresponds to about 25 GeV in generated E_T. The η dependence of the systematic effect for the jets in the first bins in Figure A.5 (left) and (right) was also

checked. As can be seen from Figure 4.4 (right) no significant η dependence of the systematic deviation was found. Therefore, it was concluded that despite some residual systematic effect at low E_T, the calibration could safely be used for L1 jet selection studies down to an E_T of 30-40 GeV. This is also the lower limit were the simulation is at all expected to be able to reproduce the upcoming experimental data.

For many of the L1 selections in the CMS/TOTEM forward physics program [38] a cutoff of 40 GeV on the calibrated E_T was used. Figure A.7 show the fractional deviation of the calibrated E_T for jets selected by such a cutoff in a QCD sample (left) and an exclusive central diffractive Higgs sample (right, m_H = 120 GeV). Gaussian fits to the QCD histograms show no deviation from zero for the mean. The small deviation from zero for the mean in the Higgs sample is only due to the kinematics of these events since only jets with E_T's upto 60 GeV are present in this sample. The upper tail in both distributions is originating from the small remnant systematic effect discussed above.

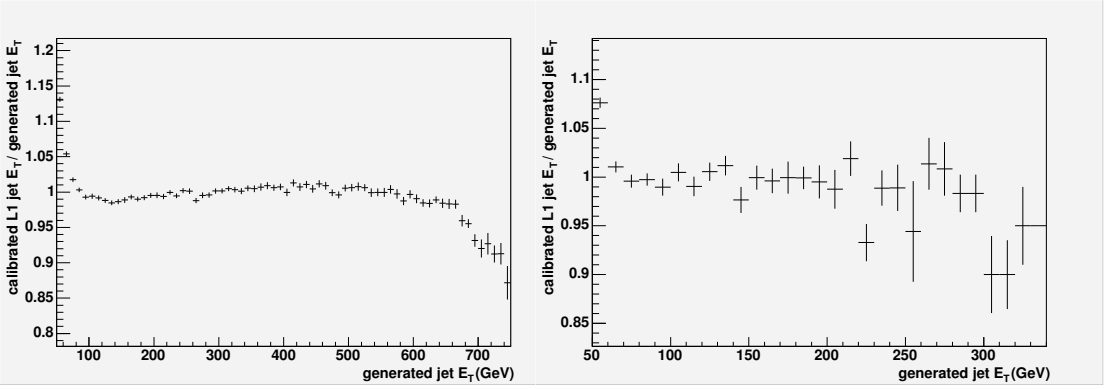

Figure A.5: The ratio of the calibrated E_T to the generated E_T as function of the generated E_T for jets in the central (left) and forward regions (right) ($|\eta| < 3.0$ and $3.0 < |\eta| < 5.1$, respectively).

Lastly, an approximate calibrated jet E_T resolution was extracted. Figure A.8 shows the width of the distribution of the ratio of the calibrated jet E_T and the generated jet E_T as a function of the generated jet E_T. The behaviour as a function of generated jet E_T is largely like expected, a convolution of a constant term $p0$ and a $\sqrt{\text{constant}/E_T}$-term, namely

$$f(E_T) = \sqrt{p0^2 + \frac{\text{constant}}{E_T}} = p0 * \sqrt{1 + \frac{p1}{E_T}}.$$

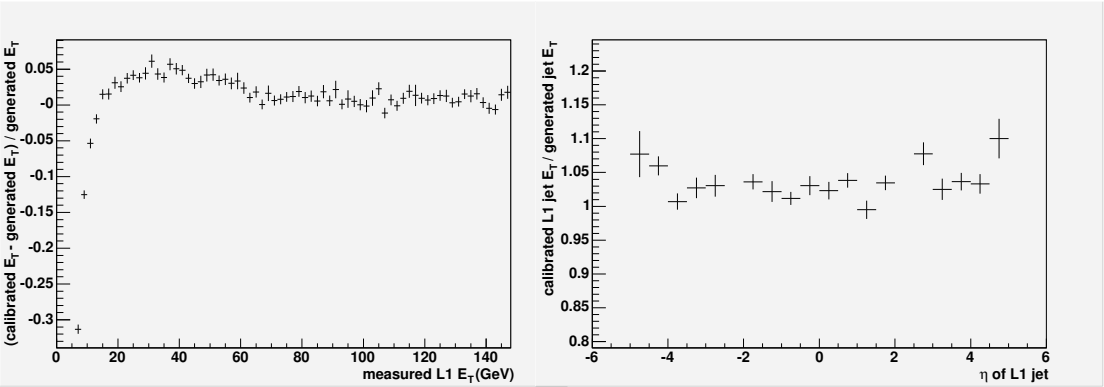

Figure A.6: Left: The fractional deviation of the calibrated E_T from the generated E_T as function of the measured L1 E_T for the low E_T part. Right: The ratio of the calibrated E_T to the generated E_T as function of the L1 jet η for jets with a generated E_T between 50 and 60 GeV.

This was ascertained by finding the best fit function of the form given above. The resulting parameters from such a fit on a sample of QCD jets with calibrated $E_T >$ 50 GeV and $|\eta| < 3.0$ were a constant term $p0 = (6.37 \pm 0.06)$ % and a poissonian term $p0 * \sqrt{p1/E_T} = (141 \pm 2)\ \%/\sqrt{E_T[\text{GeV}]}$. As can be seen from the χ^2 of the fit in Figure A.8 as well as from how well the points follow the superimposed curve, the fitted functional form doesn't describe the data well, so the extracted numbers have to be taken only as indicative. Adding a noise term proportional to the inverse of E_T didn't give any noticeable improvement to the fit.

A.6 Conclusions

In this note, calibration functions for the L1 jet transverse energy as a function of both the L1 E_T and the pseudorapidity have been extracted. The calibrations are based on a full simulation of the CMS detector, and markedly improve the quality of the reconstructed L1 jets. From a study of the remaining systematic effects at low E_T, the conclusion is drawn that the calibration can safely be used for L1 jet selection studies down to an E_T of 30-40 GeV.

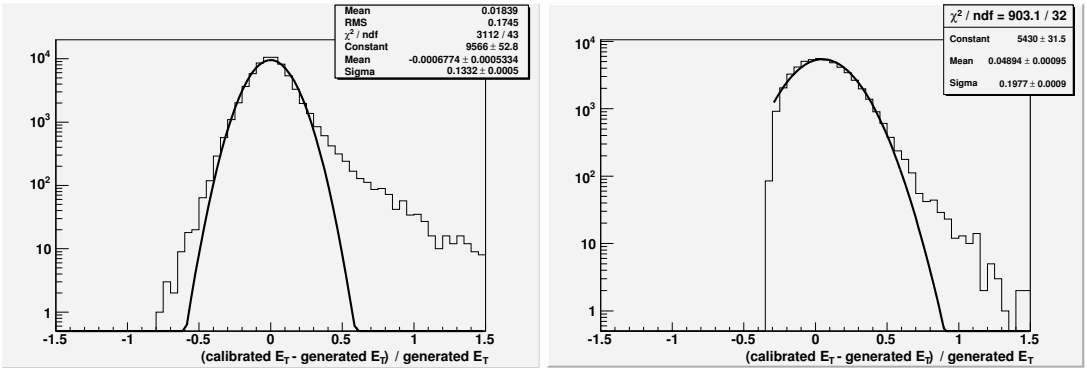

Figure A.7: Gaussian fit to the pull, i.e. the fractional deviation of the calibrated E_T from the generated E_T, for the QCD sample (left) and the ExHuME sample (right), for all jets having calibrated $E_T > 40$ GeV.

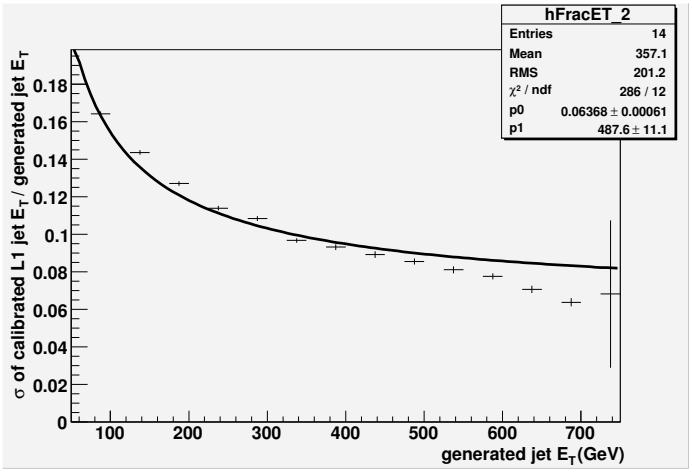

Figure A.8: Gaussian width of the distribution of the ratio of the calibrated jet E_T and the generated E_T as a function of the generated E_T for central L1 jets ($|\eta| < 3.0$). Superimposed is the best fit giving an $\sigma(E_T)/E_T = (6.37 \pm 0.06)\% \oplus (141 \pm 2)\%/\sqrt{E_T[\text{GeV}]}$. See the text on page 56 for more details.

A.7 Appendix: Calibration functions for different η-intervals

The fits for two η-intervals were presented in the text (see Figure A.2), but not all. Here is a complete list of all the double-parabolic fits in the 22 η-intervals with the values of the fitted parameters: All functions below are of the form $E_{T.gen.}^{inv.} = 2 * (E_T^{L1} -$

$par0)/(par1 + \sqrt{par1^2 - 4 * par0 * par2 + 4 * par2 * E_T^{L1}})$

To obtain the inverse function, i.e. the L1 E_T corresponding to a given generated E_T value, first find the correct η-range. Then use the above formula to find the values of generated E_T corresponding to the endpoints of the given L1 E_T ranges. Lastly, evaluate $E_{T.L1}^{fit} = par2 * E_{T.gen.}^2 + par1 * E_{T.gen.} + par0$.

Table A.2: All the double-parabolic fits in the 22 η-intervals with the values of the fitted parameters.

Name	**Value**
Interval 1 Low	(-5.115 $< \eta <$-4.439 & 6.4685 $< L1\ E_T\ (GeV) <$ 8.8757)
Par 0	8.01053
Par 1	-0.317671
Par 2	0.016347
Interval 1 High	(-5.115 $< \eta <$-4.439 & 8.8757 $< L1\ E_T\ (GeV) <$ 55.212)
Par 0	2.1871
Par 1	0.21525
Par 2	0.00415466
Interval 2 Low	(-4.439 $< \eta <$-3.839 & 6.6335 $< L1\ E_T\ (GeV) <$ 12.384)
Par 0	7.5592
Par 1	-0.29642
Par 2	0.0203854
Interval 2 High	(-4.439 $< \eta <$-3.839 & 12.384 $< L1\ E_T\ (GeV) <$ 103.66)
Par 0	-4.3132
Par 1	0.68127
Par 2	0.000257198
Interval 3 Low	(-3.839 $< \eta <$-3.33 & 6.7744 $< L1\ E_T\ (GeV) <$ 13.230)
Par 0	7.16239
Par 1	-0.226287
Par 2	0.0187485
Interval 3 High	(-3.839 $< \eta <$-3.33 & 13.230 $< L1\ E_T\ (GeV) <$ 184.21)
Par 0	-4.52182
Par 1	0.708081
Continued on next page	

Table A.2 – continued from previous page

Name	Value
Par 2	6.85266e-05
Interval 4 Low	(-3.33 $< \eta <$-3.0 & 6.7495 $< L1\ E_T\ (GeV) <$ 16.787)
Par 0	6.38369
Par 1	-0.0816137
Par 2	0.0118196
Interval 4 High	(-3.33 $< \eta <$-3.0 & 16.787 $< L1\ E_T\ (GeV) <$ 242.89)
Par 0	-6.71204
Par 1	0.704413
Par 2	2.49264e-05
Interval 5 Low	(-3.0 $< \eta <$-2.172 & 6.4465 $< L1\ E_T\ (GeV) <$ 34.351)
Par 0	5.83242
Par 1	0.000230754
Par 2	0.00611815
Interval 5 High	(-3.0 $< \eta <$-2.172 & 34.351 $< L1\ E_T\ (GeV) <$ 523.71)
Par 0	-21.9264
Par 1	0.813622
Par 2	0.00015963
Interval 6 Low	(-2.172 $< \eta <$-1.74 & 6.5503 $< L1\ E_T\ (GeV) <$ 42.008)
Par 0	5.31387
Par 1	0.0775463
Par 2	0.00460962
Interval 6 High	(-2.172 $< \eta <$-1.74 & 42.008 $< L1\ E_T\ (GeV) <$ 604.20)
Par 0	-24.2059
Par 1	0.804588
Par 2	0.000133046
Interval 7 Low	(-1.74 $< \eta <$-1.392 & 6.7761 $< L1\ E_T\ (GeV) <$ 47.774)
Par 0	4.98445
Par 1	0.143096
Par 2	0.00360696
Interval 7 High	(-1.74 $< \eta <$-1.392 & 47.774 $< L1\ E_T\ (GeV) <$ 581.51)
Par 0	-23.7496

Continued on next page

Table A.2 – continued from previous page

Name	Value
Par 1	0.775496
Par 2	0.000127374
Interval 8 Low	(-1.392 $< \eta <$-1.044 & 6.3926 $< L1\ E_T\ (GeV) <$ 48.900)
Par 0	4.31074
Par 1	0.177634
Par 2	0.00305521
Interval 8 High	(-1.392 $< \eta <$-1.044 & 48.900 $< L1\ E_T\ (GeV) <$ 553.29)
Par 0	-22.2511
Par 1	0.735743
Par 2	0.000123502
Interval 9 Low	(-1.044 $< \eta <$-0.696 & 6.8653 $< L1\ E_T\ (GeV) <$ 46.836)
Par 0	4.82439
Par 1	0.168734
Par 2	0.00353554
Interval 9 High	(-1.044 $< \eta <$-0.696 & 46.836 $< L1\ E_T\ (GeV) <$ 574.97)
Par 0	-21.4602
Par 1	0.767979
Par 2	0.000120097
Interval 10 Low	(-0.696 $< \eta <$-0.348 & 6.8110 $< L1\ E_T\ (GeV) <$ 51.220)
Par 0	4.42813
Par 1	0.205124
Par 2	0.00331642
Interval 10 High	(-0.696 $< \eta <$-0.348 & 51.220 $< L1\ E_T\ (GeV) <$ 619.72)
Par 0	-22.8945
Par 1	0.800283
Par 2	7.53879e-05
Interval 11 Low	(-0.348 $< \eta <$0.0 & 7.0323 $< L1\ E_T\ (GeV) <$ 48.651)
Par 0	4.52349
Par 1	0.215891
Par 2	0.00349897
Interval 11 High	(-0.348 $< \eta <$0.0 & 48.651 $< L1\ E_T\ (GeV) <$ 582.68)

Continued on next page

Table A.2 – continued from previous page

Name	Value
Par 0	-20.4748
Par 1	0.799887
Par 2	8.82359e-05
Interval 12 Low	(0.0 $< \eta <$0.348 & 6.8468 $< L1\ E_T\ (GeV) <$ 50.259)
Par 0	4.25144
Par 1	0.22579
Par 2	0.00337425
Interval 12 High	(0.0 $< \eta <$0.348 & 50.259 $< L1\ E_T\ (GeV) <$ 581.62)
Par 0	-21.2699
Par 1	0.805761
Par 2	7.92976e-05
Interval 13 Low	(0.348 $< \eta <$0.696 & 7.0877 $< L1\ E_T\ (GeV) <$ 48.619)
Par 0	4.88783
Par 1	0.184915
Par 2	0.00350721
Interval 13 High	(0.348 $< \eta <$0.696 & 48.619 $< L1\ E_T\ (GeV) <$ 580.11)
Par 0	-21.6829
Par 1	0.786251
Par 2	0.000104927
Interval 14 Low	(0.696 $< \eta <$1.044 & 6.5491 $< L1\ E_T\ (GeV) <$ 50.202)
Par 0	4.26682
Par 1	0.195684
Par 2	0.0032546
Interval 14 High	(0.696 $< \eta <$1.044 & 50.202 $< L1\ E_T\ (GeV) <$ 573.65)
Par 0	-22.6703
Par 1	0.77821
Par 2	0.000105258
Interval 15 Low	(1.044 $< \eta <$1.392 & 6.5835 $< L1\ E_T\ (GeV) <$ 50.922)
Par 0	4.49216
Par 1	0.179097

Continued on next page

Table A.2 – continued from previous page

Name	Value
Par 2	0.00300388
Interval 15 High	(1.044 $< \eta <$1.392 & 50.922 $< L1\ E_T\ (GeV) <$ 595.69)
Par 0	-23.3845
Par 1	0.747788
Par 2	0.000103522
Interval 16 Low	(1.392 $< \eta <$1.74 & 6.7789 $< L1\ E_T\ (GeV) <$ 50.630)
Par 0	4.88419
Par 1	0.155078
Par 2	0.00343904
Interval 16 High	(1.392 $< \eta <$1.74 & 50.630 $< L1\ E_T\ (GeV) <$ 580.32)
Par 0	-25.1323
Par 1	0.787201
Par 2	0.000111041
Interval 17 Low	(1.74 $< \eta <$2.172 & 6.6217 $< L1\ E_T\ (GeV) <$ 40.268)
Par 0	5.47166
Par 1	0.0673773
Par 2	0.00476289
Interval 17 High	(1.74 $< \eta <$2.172 & 40.268 $< L1\ E_T\ (GeV) <$ 558.51)
Par 0	-23.0453
Par 1	0.792151
Par 2	0.000157779
Interval 18 Low	(2.172 $< \eta <$3.0 & 6.6440 $< L1\ E_T\ (GeV) <$ 34.634)
Par 0	6.21302
Par 1	-0.0202949
Par 2	0.00633931
Interval 18 High	(2.172 $< \eta <$3.0 & 34.634 $< L1\ E_T\ (GeV) <$ 513.70)
Par 0	-23.1363
Par 1	0.835662
Par 2	9.84424e-05
Interval 19 Low	(3.0 $< \eta <$3.33 & 6.7513 $< L1\ E_T\ (GeV) <$ 17.255)
Par 0	6.13626

Continued on next page

Table A.2 – continued from previous page

Name	Value
Par 1	-0.0468495
Par 2	0.0108353
Interval 19 High	(3.0 $< \eta <$3.33 & 17.255 $< L1\ E_T\ (GeV) <$ 210.08)
Par 0	-6.45633
Par 1	0.688078
Par 2	0.000112404
Interval 20 Low	(3.33 $< \eta <$3.839 & 6.6990 $< L1\ E_T\ (GeV) <$ 13.284)
Par 0	6.96041
Par 1	-0.210309
Par 2	0.0184168
Interval 20 High	(3.33 $< \eta <$3.839 & 13.284 $< L1\ E_T\ (GeV) <$ 176.63)
Par 0	-4.608
Par 1	0.711495
Par 2	5.38132e-05
Interval 21 Low	(3.839 $< \eta <$4.439 & 6.6064 $< L1\ E_T\ (GeV) <$ 14.278)
Par 0	7.26157
Par 1	-0.258852
Par 2	0.0193339
Interval 21 High	(3.839 $< \eta <$4.439 & 14.278 $< L1\ E_T\ (GeV) <$ 107.77)
Par 0	-3.19043
Par 1	0.630049
Par 2	0.000731346
Interval 22 Low	(4.439 $< \eta <$5.115 & 6.4977 $< L1\ E_T\ (GeV) <$ 11.380)
Par 0	7.89381
Par 1	-0.29144
Par 2	0.0151825
Interval 22 High	(4.439 $< \eta <$5.115 & 11.380 $< L1\ E_T\ (GeV) <$ 59.728)
Par 0	0.752573
Par 1	0.308524
Par 2	0.00281229

Bibliography

[1] V. A. Khoze, A. D. Martin and M. G. Ryskin, **Eur. Phys. J. C23, 311 (2002)**.

[2] A. B. Kaidalov, V. A. Khoze, A. D. Martin and M. G. Ryskin, **Eur. Phys. J. C33, 261 (2004)**.

[3] V. Bergholm, *"Detection efficiency and mass resolution of the Higgs boson in forward diffractive scattering using the LHC"*, **Master's Thesis at the Helsinki University of Technology (2003)**.

[4] T. Mäki, *"Exclusive production of Higgs boson at LHC collider: Higgs mass measurement via leading proton detection"*, **Master's Thesis at the Helsinki University of Technology (2003)**.

[5] W. Yao et al., **J. Phys. G 33, 1 (2006)**.

[6] Y. Fukuda et al. (Super-Kamiokande Collaboration), **Phys. Rev. Lett. 81, 1562 (1998)**.

[7] J. Boger et al., **Nucl. Inst. & Meth. in Phys. Res. A449, 172 (2000)**.

[8] R. Davis, D. S. Harmer and K. C. Hoffman, **Phys. Rev. Lett. 20, 1205 (1968)**.

[9] M. Arneodo and M. Diehl, *"Diffraction for non-believers" in the proceedings of the "HERA and the LHC"-workshop*, **CERN-2005-014, 425 (2005)**.

[10] S. Weinberg, **The quantum theory of fields I (Cambridge University Press, Cambridge, 1995)**.

[11] G. F. Chew and S. C. Frautschi, **Phys. Rev. Lett. 7, 394 (1961)**.

[12] O. Brüning et al., *"LHC design report Vol. 1, the LHC Main Ring"*, **CERN 2004-003-V-1, (2004)**.

[13] C. Noels et al., *"LHC commissioning"*, **http://lhc-commissioning.web.cern.ch/lhc-commissioning/, (2006); accessed Sep. 26th, 2006**.

[14] D. Acosta, *"CMS TDR 8.1"*, **CERN/LHCC 2006-001, (2006)**.

[15] M. G. Albrow et al., *"FP420 : An R&D Proposal to Investigate the Feasibility of Installing Proton Tagging Detectors in the 420 m Region of the LHC"*, **CERN/LHCC 2005-025, (2005)**.

[16] G. 't Hooft, **Rev. Mod. Phys. 72 (2000) 333** [Erratum-ibid. **74** (2003) 1343].

[17] P. W. Higgs, **Phys. Rev. Lett. 13, 508 (1964)**.

[18] J. Goldstone, **Nuovo Cim. 19, 154 (1961)**.

[19] J. Ellis, M. K. Gaillard and D. V. Nanopoulos, **Nucl. Phys. B106, 292 (1976)**.

[20] M. Spira, **Fortsch. Phys. 46, 203 (1998)**.

[21] B. W. Lee, C. Quigg and H. B. Thacker, **Phys. Rev. D16, 1519 (1977)**.

[22] CMS Collaboration, *"CMS Outreach Physics Plots"*, **http://cmsinfo.cern.ch/outreach/CMSdocuments/CMSplots/CMSplots.html, (2006); accessed May 17th, 2006.**

[23] K. Abe et al., *"Particle Physics Experiments at JLC: ACFA Linear Collider Working Group Report"*, **KEK Report 2001-011, (2001)**.

[24] S. Schael et al., **Phys. Rept. 427, 257 (2006)**.

[25] J. Kalliopuska et al., *"TOTEM forward measurements: exclusive central diffraction", in the Proceedings of the "HERA and the LHC"-workshop*, **CERN-2005-014, 448 (2005)**.

[26] A. B. Kaidalov, V. A. Khoze, A. D. Martin and M. G. Ryskin, **Eur. Phys. J. C31, 387 (2003)**.

[27] V. A. Khoze, A. D. Martin and M. G. Ryskin, **Eur. Phys. J. C26, 229 (2002)**.

[28] M. Boonekamp, C. Hogg, J. Monk, A. Pilkington and M. Tasevsky, *"Monte Carlo generators for central exclusive diffraction", in the Proceedings of the "HERA and the LHC"-workshop*, **CERN-2005-014, 482 (2005)**.

[29] M. Grothe, *"L1 jet calibration"*, **http://indico.cern.ch/conferenceDisplay.py ?confId=a044893, LPC Trigger Meeting (Nov. 5th, 2004); accessed Sep. 26th, 2006**.

[30] T. Sjöstrand et al., **Comp. Phys. Comm. 135, 238 (2001)**.

[31] V. A. Petrov, R. A. Ryutin, A. E. Sobol and J.-P. Guillaud, *"EDDE Monte Carlo event generator."*, **http://arxiv.org/abs/hep-ph/0409180 (2004); accessed Sep. 26th, 2006**.

[32] J. Monk and A. Pilkington, **Comp. Phys. Comm. 175, 232 (2006)**.

[33] M. Schröder, *"CMS Detector Simulation Project OSCAR"*, **CMS Internal Note 1999-036, (1999)**.

[34] D. Stickland, *"CMS Reconstruction Software: The ORCA project"*, **CMS Internal Note 1999-035, (1999)**.

[35] R. Brun and F. Rademakers, **Nucl. Inst. & Meth. in Phys. Res. A389, 81 (1997)**.

[36] S. Vanini et al., *"2E33 Trigger Tables for PTDR, volume 2"*, **CMS Note AN-2006/085, (2006)**.

[37] M. Arnodeo et al., with F. Oljemark, *"Diffractive Higgs: CMS/TOTEM Level-1 Trigger Studies" in the proceedings of the "HERA and the LHC"-workshop*, **CERN-2005-014, 455 (2005)**.

[38] M. Grothe et al., *"Triggering on forward physics"*, TOTEM Note **2006/01** CMS Note **2006/054** (2006).

[39] S. Abdullin, S. Arcelli, S. C. Eno, A. Krokhotine and S. Kunori, *"Energy corrections for QCD jets"*, **CMS Internal Note 2001/001, (2001)**.

HELSINGIN YLIOPISTO
HELSINGFORS UNIVERSITET
UNIVERSITY OF HELSINKI

Tiedekunta/Osasto – Fakultet/Sektion – Faculty	Laitos – Institution – Department
Matematisk-naturvetenskapliga	Institutionen för fysikaliska vetenskaper

Tekijä – Författare – Author
Fredrik Robert Oljemark

Työn nimi – Arbetets titel – Title
First level triggering of diffractively produced low-mass Higgs at The Large Hadron Collider

Oppiaine – Läroämne – Subject
Fysik

Työn laji – Arbetets art – Level	Aika – Datum – Month and year	Sivumäärä – Sidoantal – Number of pages
Pro gradu-avhandling	27.9.2006	66

Tiivistelmä – Referat – Abstract
Higgs-bosonen är den enda oupptäckta partikeln i standardmodellen, som beskriver de elementära partiklarnas växelverkan. Higgs-sökningarna vid LEP-experimenten gav en undre gräns, 115 GeV, för dess massa. Om Higgs-bosonens massa är nära LEPs undre gräns är central diffraktiv Higgs-produktion en experimentellt attraktiv Higgs-sökningsprocess vid Large Hadron Collider i CERN. I denna avhandling har första nivån av triggern studerats i detalj för centrala diffraktiva Higgs-händelser. Målet är att optimera effektiviteten för signalen samtidigt som frekvensen av accepterade händelser hålls på en acceptabel nivå för datauppsamlingssystemet. Undersökningarna har fokuserats på en Higgs-boson med en massa på 120-140 GeV. Olika krav baserade på kombinationer av de på första trigger-nivån rekonstruerade myonerna och/eller partikelskurarna ("jets") har granskats i avhandlingen.

Slutsatsen av denna avhandling är att det är möjligt att spara ca. 8% av de diffraktiva Higgs-boson-händelserna, ifall Higgs sönderfaller mestadels till ett b-anti-b kvarkpar, och ca. 18% ifall Higgs sönderfaller mestadels till ett W^+W^- boson-par, med hjälp av de redan existerande en- och två-myon-triggerna. Genom att ta i bruk en ny första nivåns trigger baserat på en myon plus en partikelskur kan man öka acceptansen för händelser med Higgs-sönderfall till ett b-anti-b kvarkpar med hälften, så att trigger-effektiviteten blir ca. 12%.
Ett antal andra krav granskades också men dessa visade sig vara endast av marginell betydelse för triggereffektiviteten. Dessutom utvecklades en metod för att korrigera den transversella energin rekonstruerad för partikelskurarna på den första trigger-nivån så att den bättre skulle motsvara den verkliga transversella energin för partikelskurarna.

Avainsanat – Nyckelord – Keywords
Partikelfysik, Higgs, Central diffraktion, LHC

Säilytyspaikka – Förvaringställe – Where deposited

Muita tietoja – Övriga uppgifter – Additional information

HELSINGIN YLIOPISTO
HELSINGFORS UNIVERSITET
UNIVERSITY OF HELSINKI

Tiedekunta/Osasto – Fakultet/Sektion – Faculty	Laitos – Institution – Department
Faculty of Science	Department of Physical Sciences

Tekijä – Författare – Author
Fredrik Robert Oljemark

Työn nimi – Arbetets titel – Title
First level triggering of diffractively produced low-mass Higgs at The Large Hadron Collider

Oppiaine – Läroämne – Subject
Physics

Työn laji – Arbetets art – Level	Aika – Datum – Month and year	Sivumäärä – Sidoantal – Number of pages
Master's Thesis	27.9.2006	66

Tiivistelmä – Referat – Abstract
The Higgs boson is the only Standard Model particle that has not yet been found. Higgs searches at the experiments at LEP have given a lower limit to the Higgs mass, 115 GeV. If the Higgs mass is near this lower limit, one of the experimentally more favourable production processes at the Large Hadron Collider at CERN for a Higgs boson, is the central diffractive process. In this thesis, different first level trigger selection criteria have been studied, which use muon and/or jet signatures to retain a significant fraction of diffractive Higgs events while still keeping the accepted event rate at an acceptable level. This thesis studied Higgs bosons with masses between 120-140 GeV.

The conclusions of this thesis are that the already implemented one and two muon triggers have a signal efficiency of 8% for Higgs decaying to b-anti-b quark pairs, and 17% for Higgs decaying to W^+W^- bosons. By adding a trigger combining a muon and a jet, one can increase this efficiency to around 12 % for the b-anti-b quark pair decay. A number of other criteria were also considered, but turned out to improve the signal efficiency only marginally. In addition, a method to correct the first-level measurements of transverse jet energy so as to better correspond to the real transverse jet energy is developed is the thesis.

Avainsanat – Nyckelord – Keywords
Particle Physics, Higgs, Central Diffraction, LHC

Säilytyspaikka – Förvaringställe – Where deposited

Muita tietoja – Övriga uppgifter – Additional information